JGR Earth Surface

RESEARCH ARTICLE
10.1029/2018JF004790

Predicting Climate-Driven Coastlines With a Simple and Efficient Multiscale Model

José A. A. Antolínez[1,2], Fernando J. Méndez[1], Dylan Anderson[3], Peter Ruggiero[3], and George M. Kaminsky[4]

[1]Departamento de Ciencias y Técnicas del Agua y del Medio Ambiente, E.T.S.I. de Caminos, Canales y Puertos, Universidad de Cantabria, Santander, Spain, [2]Unit Marine and Coastal Systems, Deltares, Delft, The Netherlands, [3]College of Earth, Ocean, and Atmospheric Sciences, Oregon State University, Corvallis, OR, USA, [4]Washington Department of Ecology, Olympia, WA, USA

Key Points:
- A new coastal evolution model (COCOONED) combines effects from longshore and cross-shore transport, dune erosion, and sediment supply
- COCOONED evolves shorelines based on climate variability in both waves and water levels
- COCOONED is applied in Grays Harbor County, Washington, USA, for 35 years and reveals shoreline responses at multiple scales of variability

Correspondence to:
J. A. A. Antolínez,
jose.antolinez@deltares.nl

Citation:
Antolínez, J. A. A., Méndez, F. J., Anderson, D., Ruggiero, P., & Kaminsky, G. M. (2019). Predicting climate-driven coastlines with a simple and efficient multiscale model. *Journal of Geophysical Research: Earth Surface*, *124*, 1596–1624. https://doi.org/10.1029/2018JF004790

Received 19 JUN 2018
Accepted 21 APR 2019
Accepted article online 29 APR 2019
Published online 26 JUN 2019

Abstract Ocean-basin-scale climate variability produces shifts in wave climates and water levels affecting the coastlines of the basin. Here we present a hybrid shoreline change—foredune erosion model (A COupled CrOss-shOre, loNg-shorE, and foreDune evolution model, COCOONED) intended to inform coastal planning and adaptation. COCOONED accounts for coupled longshore and cross-shore processes at different timescales, including sequencing and clustering of storm events, seasonal, interannual, and decadal oscillations by incorporating the effects of integrated varying wave action and water levels for coastal hazard assessment. COCOONED is able to adapt shoreline change rates in response to interactions between longshore transport, cross-shore transport, water level variations, and foredune erosion. COCOONED allows for the spatial and temporal extension of survey data using global data sets of waves and water levels for assessing the behavior of the shoreline at multiple time and spatial scales. As a case study, we train the model in the period 2004–2014 (11 years) with seasonal topographic beach profile surveys from the North Beach Sub-cell (NBSC) of the Columbia River Littoral Cell (Washington, USA). We explore the shoreline response and foredune erosion along 40 km of beach at several timescales during the period 1979–2014 (35 years), revealing an accretional trend producing reorientation of the beach, cross-shore accretional, and erosional periods through time (breathing) and alternating beach rotations that are correlated with climate indices.

1. Introduction

Coastlines are among the most dynamic environments on Earth. The natural processes that shape these environments are driven by both episodic high-intensity events (e.g., storm surge flooding and storm waves) and daily modal wind, wave, and tidal conditions, which operate over longer timescales and drive chronic shoreline erosion/accretion. Earth's climate exhibits cycles, including sequencing and clustering of storm events, and seasonal, interannual, and decadal oscillations of various sorts. These cycles are superimposed on an accelerating background climate change arising from human activities (IPCC, 2013). Each of these climate signals—the cycles and the trends—will tend to cause shifts in coastline position and planview shape (e.g., Antolínez et al., 2018; Coco et al., 2014; Davidson et al., 2010; Moore et al., 2013; Ruggiero, Buijsman, et al., 2010; Ruggiero et al., 2016; Vitousek, Barnard, & Limber, 2017). Accelerated sea level rise (SLR) is also occurring and the associated change in sediment transport patterns can lead to long-term shoreline erosion (e.g., Bruun, 1962; Cowell, Stive, Niedoroda, Swift, et al., 2003; Cowell, Stive, Niedoroda, Vriend, et al., 2003; Moore et al., 2010; Ranasinghe & Stive, 2009; Wolinsky & Murray, 2009).

Approximately 1 billion of the world's population will live in the coastal zone by the end of the 21st century (Neumann et al., 2015). Beaches act as a natural form of defense, protecting people and infrastructure from flooding and wave action (Tonnon et al., 2018). They play a strong role in the economy of many regions (Kildow et al., 2014), providing recreational activities, sports, and tourism. Beaches are also important ecosystems where habitats can be influenced by climate change, nearshore morphology, invasive beachgrasses and the foredunes they create, changes in foredune shape as a result of restoration, and other coastal management actions (Biel et al., 2017; Seabloom et al., 2012). Changes in the position of the shoreline over years to decades can be drastic and costly. Thus, reliable coastal evolution predictions in both the short and long terms have become crucial for adaptation planning in anticipation of climate change and SLR.

Nevertheless, understanding and modeling the short- and long-term behavior of the coastal zone remains a significant challenge. While many modeling techniques are available, sediment transport models often lack robust governing equations describing small-scale processes such as the motion of individual sand grains. This is due to the complex dynamics of the media in which these processes develop (i.e., hydrodynamics), the difficulty of reproducing interactions between discrete particles and the manner in which particles self-organize to generate patterns that in turn influence hydrodynamics (Cheng et al., 2017). Therefore, sediment transport models often rely on equations obtained from a combination of different physical experiments.

Three approaches are common for modeling coastal evolution, including data driven, process driven, and physics driven models. Data-driven models, also known as empirical models, attempt to explain shoreline change from observed behavior (Dolan et al., 1978; Fenster & Dolan, 1994; Miller & Dean, 2007a, 2007b; Ruggiero et al., 2016; van de Lageweg et al., 2013). Although they are the most representative of morphological processes, they are limited by the extent and frequency of available historical data. Process-driven models characterize the dominant physical processes shaping coastlines such as gradients in longshore sediment transport (LST) (Ashton et al., 2001, 2002; Ashton & Murray, 2006a, 2006b; Arriaga et al., 2017; Falqués et al., 2017; Hanson, 1989; Idier et al., 2011; Kaergaard & Fredsoe, 2013a, 2013b; Murray & Ashton, 2013), wave-driven cross-shore shoreline change (Yates et al., 2009, 2010; Davidson et al., 2010, 2013; Splinter et al., 2013, 2014), beach profile response to water levels and waves (Aagaard, 2014; Kriebel & Dean, 1993; Miller & Dean, 2004; Larson et al., 2016; Patterson & Nielsen, 2016), and profile adjustment due to SLR (Bruun, 1962) without solving complex governing equations as physics-driven models do. Process-driven models have been proven reliable and computational inexpensive; however, they usually focus on solving a single physical process. The models of Hanson et al. (2010), Larson et al. (2016), and Palalane et al. (2016) are an exception as they incorporate several physical processes trying to include beach and foredune change in response to cross-shore processes of foredune growth by wind and foredune erosion (FDE) by storms, and by gradients in longshore sand transport that will alter shoreline position. Vitousek, Barnard, Limber, Erikson, et al. (2017) have introduced a hybrid transect-based model composed of a one-line longshore transport model, a cross-shore equilibrium shoreline model, and a sea level-driven shoreline recession model. The model of Vitousek, Barnard, Limber, Erikson, et al. (2017) covers a wide range of important processes for understanding coastal behavior, and the implemented data assimilation technique has improved the model's accuracy in comparison with measurements. However, in this model water level variations other than SLR do not affect computed shoreline erosion rates and during conditions of very low wave energy (or no energy) and SLR, the profile still readjusts at a constant rate given by the "Bruun Rule" (Bruun, 1962). Recently, Robinet et al. (2018) presented a novel model integrating alongshore and cross-shore wave processes solved on a 2-D planview grid schematization that allows for the evolution of strong curvatures on the shoreline planview, in a similar fashion as in Ashton et al. (2001) for the longshore component and with an adapted version of Davidson et al. (2013) for the cross-shore component. Furthermore, wave processes in Robinet et al. (2018) are solved with the SWAN model (Booij et al., 1999). Hence, it is possible to account for the effects of complex bathymetry in wave propagation. Nevertheless, it does not include readjustment of the shoreline position due to water level variations.

Physics-driven models intend to solve governing equations (e.g., conservation of mass, momentum, and energy) for hydrodynamics, waves, sediment transport, and morphology. This class of models is robust but usually requires high computational effort. Therefore, techniques to increase computational efficiency have been developed such as model reduction of complex systems focusing in the relevant processes (Cowell, Stive, Niedoroda, Vriend, et al., 2003; de Vriend et al., 1993), morphological acceleration and consequent hydrodynamic run time reduction (Roelvink, 2006), and input reduction techniques (Antolínez et al., 2016; Walstra et al., 2013). Nevertheless, physics-driven models do not necessarily offer more accurate results than process-driven models (French et al., 2016; Murray, 2007).

In this paper we present a novel shoreline evolution model (A COupled CrOss-shOre, loNg-shorE, and foreDune evolution model, COCOONED), which combines a hybrid nearshore propagation of offshore waves using a physics-driven model, data mining and statistical methods following Antolínez et al. (2018), and a process-driven coastal model combining (1) longshore transport and shoreline change due to waves with a one-line approach similar to Vitousek and Barnard (2015), (2) cross-shore transport and equilibrium shoreline change due to waves and varying water levels (e.g., SLR, monthly sea level anomalies, and storm surge) using a modified version of the Miller and Dean (2004) model, (3) FDE using a modified version of the

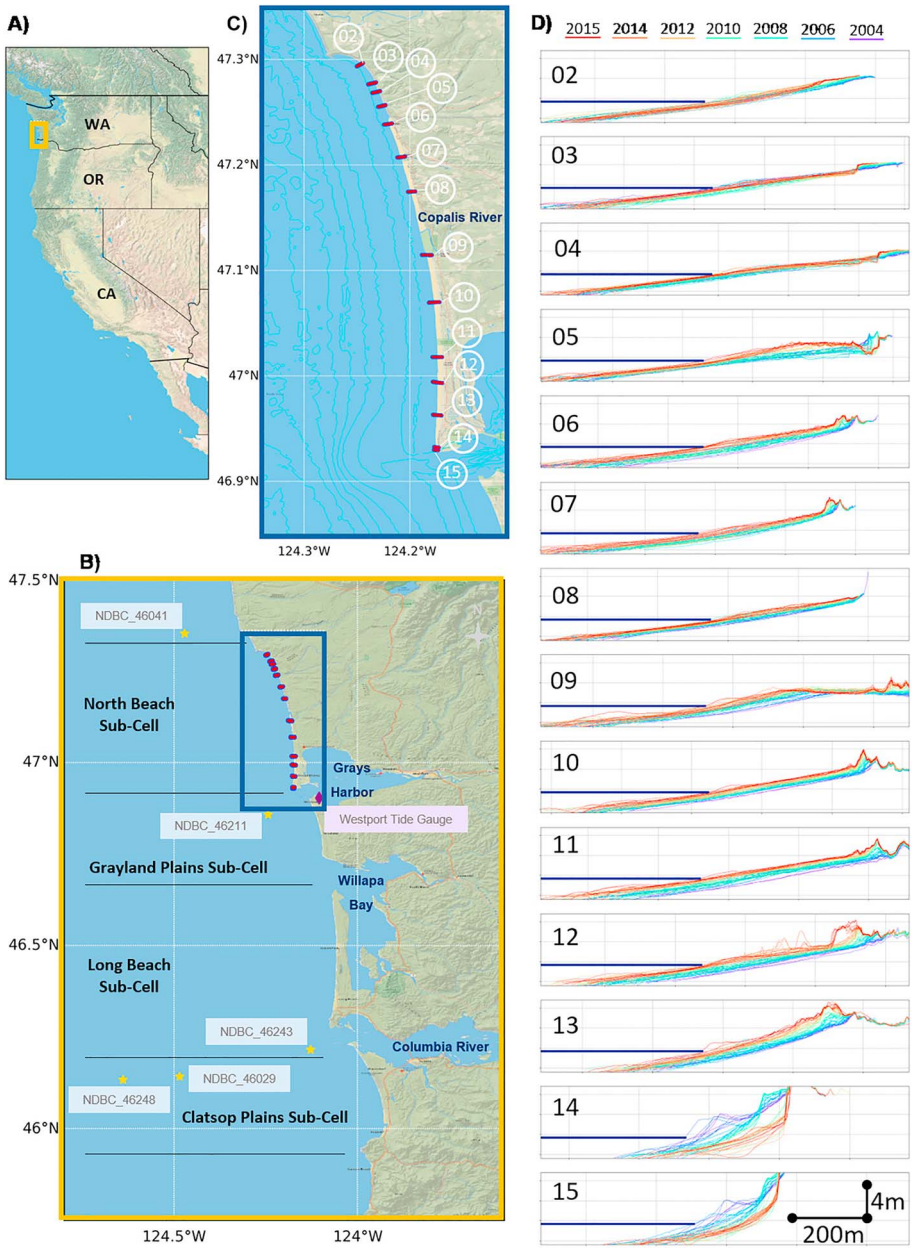

Figure 1. (a) The Columbia River Littoral Cell and the study site (North Beach Subcell) in Washington State, U.S. West Coast. In panels (b) and (c) the pink lines represent the location of the transects where seasonal beach profile data are available. In panel (b) the yellow stars represent the location of the buoys used for validating the nearshore wave transformation model and the purple diamond locates the tide gauge used for extracting the water levels. Panel (d) shows the profile data collected in the period 2004–2015 for each of the transects, the color scale (rainbow) represents the temporal evolution from 2004 (purple) to 2015 (red). The blue line represents the 2.1-m elevation contour relative to NAVD88 (MLLW equivalent in Grays Harbor County).

model proposed by Mull and Ruggiero (2014) based on Kriebel and Dean (1993), and (4) the inclusion of profile adjustment by sediment supply. With this model we account for the combined effects of waves, varying water levels, and sediment supply in shoreline and FDE covering a wide range of spatial and temporal scales, including sequencing and clustering of storm events, and seasonal, interannual, and decadal oscillations. We also model the influence of FDE on shoreline erosion rates as well as the influence of sediment supply, which can be the major driver in prograding beach morphodynamics.

COCOONED allows us to explore the coastal response to long periods of regular or anomalous atmospheric and oceanographic conditions at basin scale, improving our ability to assess the exposure of large, densely

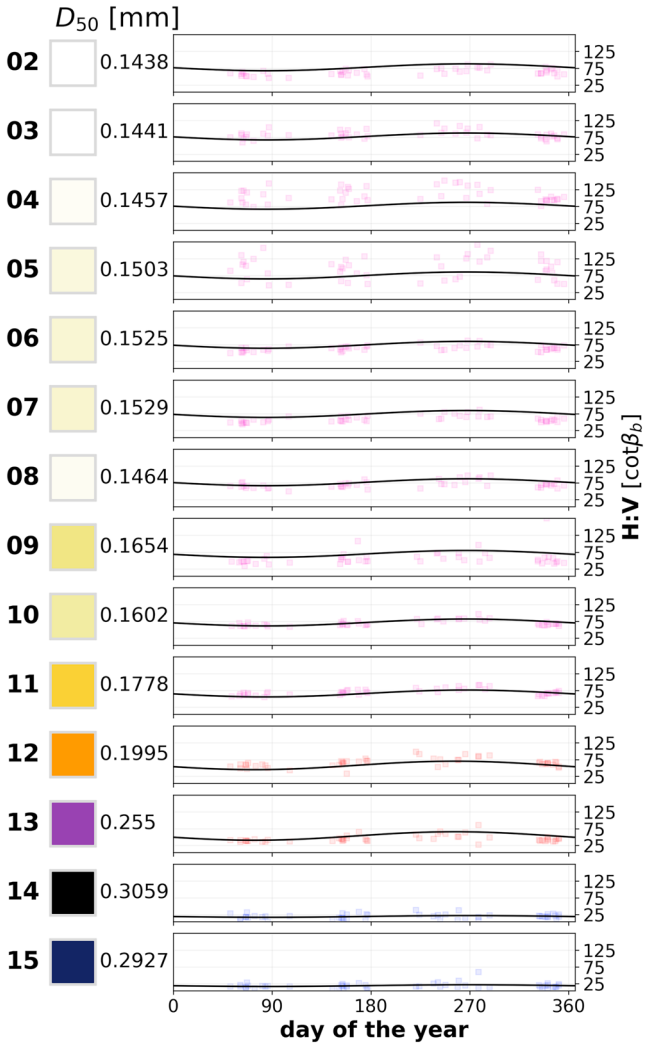

Figure 2. The left panel shows the alongshore variability in the representative sediment grain size (defined by the temporal mean median size diameter, D_{50}[mm]) along the transects in the North Beach Subcell. "Transect 02" is located in the north, and "Transect 15" in the south near the Grays Harbor North Jetty. The right panel shows the seasonal variability in the modeled backshore slopes (tan β_b, black lines) and in the observations (squared dots) for each of the transect locations. The x axis represents the day of the year. The colors of the squared dots represent the belonging group according to the sediment grain size distribution classification defined in Appendix B (see also Figure B1). The transparency of the dots is proportional to the number of sample points at the same location (the darker the more data points).

populated regions to coastal flooding and erosion hazards. As a case study we apply COCOONED in the North Beach Sub-cell (NBSC) of the Columbia River Littoral Cell (CRLC; Washington, USA; see Figure 1) to explore the shoreline response and FDE along 40 km at different timescales (storm, seasonal, interannual, and decadal) in the period 1979–2014 (35 years). We use 11 years (2004–2014) of seasonal topo-profile surveys for training the model coefficients.

Section 2.1 of this manuscript starts with a brief introduction on the morphodynamic behavior of the study area (NBSC). Section 2.2 explains the collection of the morphological data used through the paper. Section 3 develops the offshore to nearshore wave propagation and the coastal evolution model including the numerical implementation. In section 4 we explain the application of COCOONED in the study area, the model parameters, and constant rates chosen for optimizing the predictions in the training period, and we comment on the results obtained for the hindcast period at multiple spatial and temporal scales. In section 5 we introduce model limitations, the interaction between processes in COCOONED, and we discuss the correlation found between climate variability and shoreline response. We summarize conclusions in section 6.

2. The NBSC of the CRLC

2.1. Study Area

The CRLC extends between Tillamook Head, Oregon and Point Grenville, Washington (southern and northern black horizontal lines in Figure 1) and consists of four concave-shaped prograded barrier plain subcells separated by the Columbia River, Willapa Bay, and Grays Harbor estuaries (Figure 1). The CRLC is the only extensive stretch of shoreline on the U.S. west coast that has naturally accumulated sufficient sand volumes for the beach to advance seaward (Kaminsky et al., 2010; Ruggiero et al., 2016).

NBSC spans about 50 km between the Grays Harbor North Jetty and Point Grenville. Beach slopes in the subcell are steepest at the southern profiles and decrease to the north (Figure 1D). Median grain sizes are larger near the mouth of Grays Harbor and decrease to the north where the finest sediment in the CRLC, with a median grain size of about 0.12 mm, can be found (Figure 2). Foredune crest elevations are highest at the southern end of the sub-cell (7- to 8-m elevation and 2.5–3.5 m high) and decrease in height to the north (5- to 6-m elevation and 1.5–2 m high). North of the Copalis River (approximately nearby "Transect 07"), the beaches are backed by cliffs or bluffs. Over the long-term (1800s through 2002), the average shoreline change rate, 4.4 m/year, for the NBSC was the most progradational of any littoral cell within the U.S. Pacific Northwest. The maximum rate reported (Ruggiero et al., 2013) was 21.8 m/year. Shoreline progradation rates are high in the recent decades (1960s through 2002) as well, with a sub-cell-averaged rate of 4.2 m/year. A clear break in shoreline change trend at the Copalis River is consistent in time, with higher rates of shoreline progradation to the south of the river than to the north (Ruggiero et al., 2013).

The wave climate in the CRLC is highly energetic, with annual deep water significant wave heights and periods averaging 2 m and 10 s, respectively. Winter months (November through February) are characterized by high, long-period west-southwesterly waves (3 m in height and 12–13 s in period) and winter storms producing wave heights of 8–10 m. Smaller waves (1.2 m and 8 s), lower water levels, and wind and waves from the west-northwest are the typical summer (May through August) conditions. Tides along the CRLC are mixed semidiurnal with a 2- to 4-m tide range. Water levels also have a distinct seasonal cycle, measuring approximately 20 cm higher during the winter than during summer months. In the U.S. Pacific Northwest,

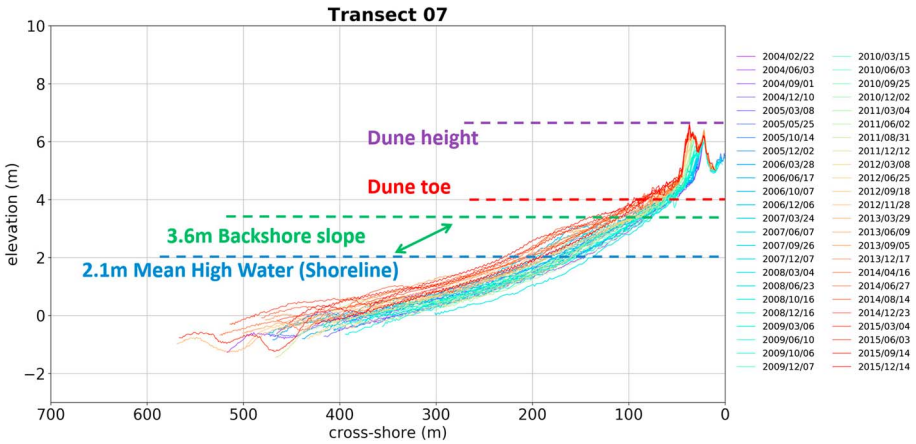

Figure 3. Example schematization of the active beach and foredune profile by the shoreline position (2.1-m elevation), the backshore slope (defined between 2.1- and 3.6-m elevation), and the foredune toe and crest elevations at "Transect 07" on the observed profiles. The elevations are referred to NAVD88 (MLLW equivalent in Grays Harbor County).

strong El Niño episodes are associated with an increased frequency of storm tracks from the south-southwest and higher than normal sea levels (Barnard et al., 2017; Kaminsky et al., 1998; Komar et al., 2011; Ruggiero, Komar, et al., 2010).

In the CRLC, jetties also affect seasonally reversing LST patterns; however, the primary driver of jetty-induced shoreline change has been the onshore transport and welding to the shoreline of the flanks of the ebb-tidal deltas (Kaminsky et al., 2010), and for this reason these beaches are highly progradational.

The U.S. Pacific Northwest has some of the largest coastal foredune systems in the country, with foredune-backed beaches covering approximately 45% of the Oregon and Washington coastlines. Storm surge is limited due to the geometry of the continental shelf (Bromirski et al., 2003), and foredunes are often relatively tall compared with high water levels. Therefore, CRLC foredunes are typically in the collision regime (water level exceeding the foredune toe but not overtopping; Sallenger, 2000) during storms, resulting in some areas being particularly susceptible to erosion, with inundation being relatively rare.

2.2. Observations

Upper shoreface, nearshore, beach, and foredune evolution within the NBSC is being monitored with Real Time Kinematic Differential Global Positioning System surveying techniques (Ruggiero et al., 2005). Topographic beach profiles are collected quarterly (1997 to present) at 14 locations distributed alongshore approximately 3 km apart (Figure 1). Topographic beach profiles are measured by walking from the landward side of the primary foredune ridge, over the foredune crest, to wading depth during spring low tides. Annually, a personal water craft based Coastal Profiling System is used to measure nearshore morphology each summer at representative transects to depths seaward of measurable annual change (approximately −12 m MLLW; Di Leonardo & Ruggiero, 2015; Ruggiero et al., 2005). In situ beach measurements have been occasionally augmented by airborne lidar data (Ruggiero et al., 2013).

For the coastline and FDE modeling described here, morphometrics from the data set have been extracted for the period 2004–2014. Shoreline position is identified as the 2.1-m elevation contour relative to NAVD88 (MLLW equivalent in Grays Harbor County, Figure 3). The backshore slope is computed as the mean slope between 2.1- and 3.6-m elevation, and the foredune toe and foredune crest elevations are extracted manually (shown schematically in Figure 3 with backshore slope variability shown in Figure 2).

Sediment samples were collected at each transect every summer between 1997–2004 (Figure 2). Surface grab samples were collected by hand (typically several hundred grams of beach sand) at four locations along each beach profile, including the crest of the foredune ridge, at the foredune toe, at midbeach, and within the swash zone at low tide. Grain size distributions were determined with American Society for Testing and Materials—approved dry sieves at quarter-phi intervals following U.S. Environmental Protection Agency protocols for sediment analyses (Tetra Tech et al., 1986).

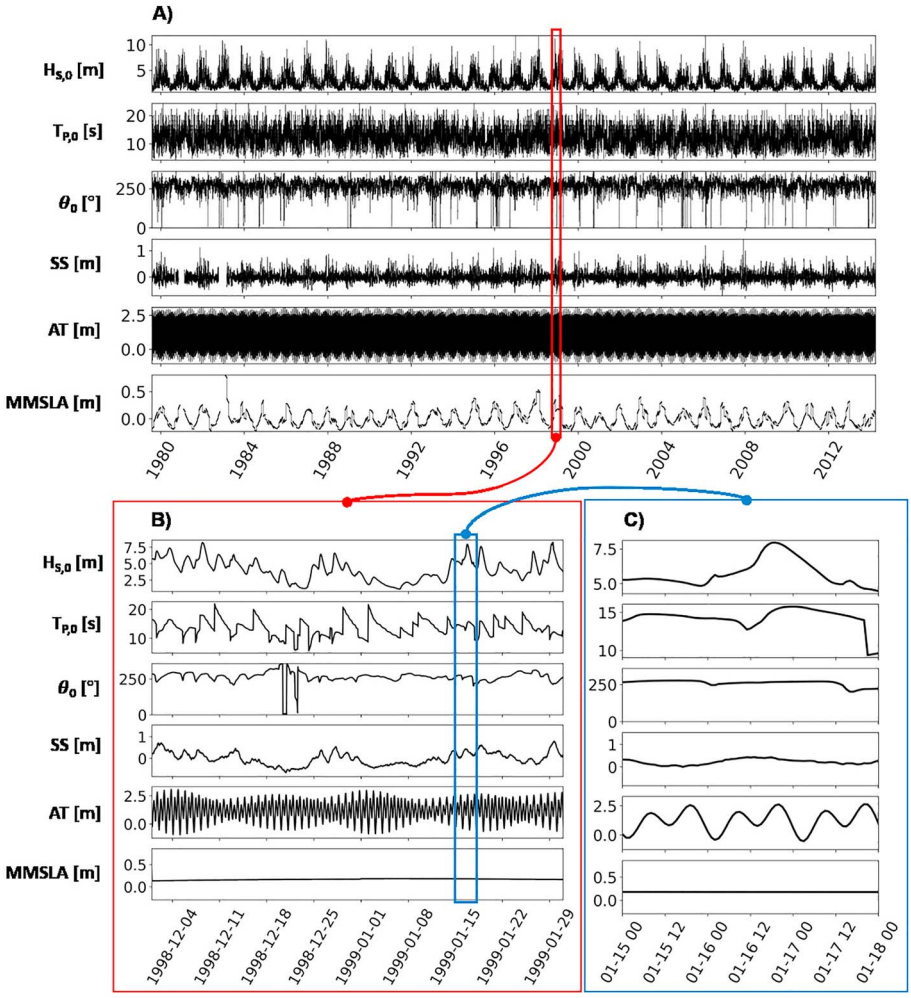

Figure 4. Panel (a) shows the temporal series of hourly environmental forcing. $H_{S,0}$ is the significant wave height, $T_{P,0}$ the peak period, and θ_0 the mean direction from GOW2. *SS* is the storm surge, *AT* the local astronomical tide, and *MMSLA* the monthly mean sea level anomalies taken from a tide gauge located in Westport (WA). Panel (b) shows the monthly variations during January 1999. Panel (c) highlights the hourly resolution of the forcing between the 15th to the 18th of January during a storm.

We use the Global Ocean Waves (GOW2) hindcast (Perez et al., 2017) as boundary conditions to model wave propagation to the nearshore. The GOW2 hindcast is developed running the WAVEWATCH III wave model in a multigrid two-way nesting configuration from 1979 onward. The multigrid includes a global grid of 0.5° ×0.5° degree spatial resolution, specific grids configured for the Arctic and the Antarctic polar areas, and a grid of higher resolution (about 25 km) for all coastal locations at depths shallower than 200 m. Available outputs include hourly sea state parameters (e.g., H_S, T_P, and θ) and series of 3-hr spectra. This data set is extracted at a point (Lon = 126° W, Lat = 46° N) located in deep water close to National Data Buoy Center buoy 46089.

We use buoy data from the National Data Buoy Center of the National Oceanic and Atmospheric Administration for validating wave hindcast results and our wave propagations (Figure 1b).

Finally, we use measured water levels from a tide gauge located in Westport, WA (inner Grays Harbor). These account for astronomical tide, storm surge, and monthly sea level anomalies. The separation of the various components comprising the total water levels is performed following Serafin et al. (2017); see Figure 4.

3. Model Development

3.1. Hybrid Nearshore Propagation of Ocean Waves From Deep Water Wave Hindcast

The nearshore wave propagation of waves consists of a hybrid downscaling (Camus et al., 2011) of a representative subset of sea state conditions selected in deep water, consisting of hourly significant wave height

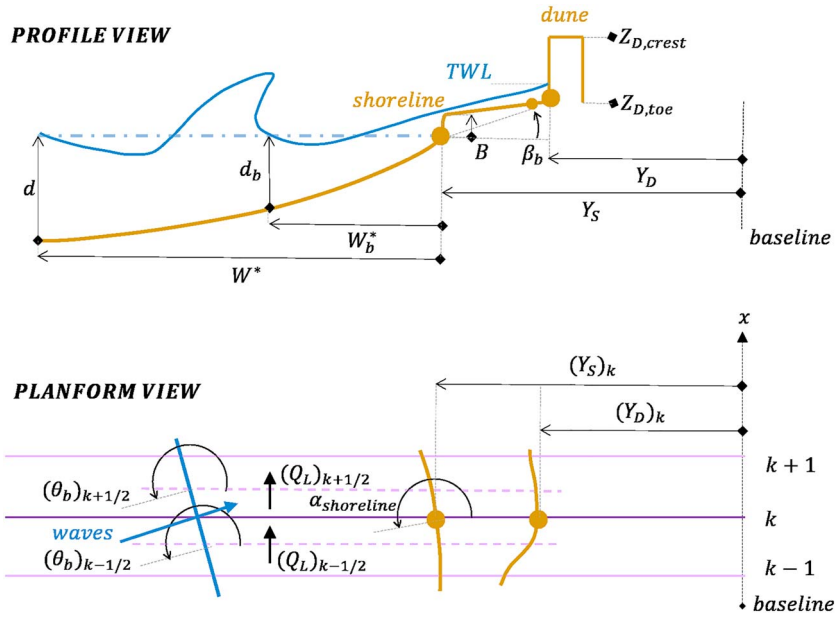

Figure 5. Schematic showing the setup of the coastal evolution model.

($H_{S,0}$), peak period ($T_{P,0}$), and mean direction (θ_0); see section 2.2, Figure 4. Interpolation functions are trained from the offshore boundary wave climate series to reconstruct continuous hourly wave climate series at a depth relevant to the shoreline change modeling (in this study 20-m water depth). The methodology has been previously applied in other long-term morphological studies (Antolínez et al., 2018). Further details on the hybrid nearshore wave propagation are given in Appendix A).

3.2. Integrated Longshore and Cross-Shore Model

The process-driven coastal model solves for both shoreline evolution and FDE. It drives changes at several temporal and spatial scales, by modeling the effects of waves and water levels, which influence the coastal morphology (represented here by the shoreline and the foredune; Figure 5). A schematic of the coastline evolution model is shown in Figure 5. The governing equations of our model for shoreline evolution and FDE are two partial differential equations describing an aggregation of several process-driven models including (1) an alongshore transport "one-line" model accounting for the influence of waves reaching the coast with a certain incident angle (first term on the right side of equation (1)), (2) a cross-shore equilibrium shoreline model accounting for the effect of the wave action and the presence of varying water levels (second term equation (1)), (3) a FDE model accounting for FDE due to waves and water level oscillations (equations (2) and (3)), and (4) a term including the influence of sediment supply (third termon the right side of equation 1).

$$\frac{\partial Y_S}{\partial t} = \frac{-1}{d}\frac{\partial Q_L}{\partial x} + K_C(Y_{S,eq} - Y_S) + \frac{-1}{d}\left(q_x + q_y\right), \tag{1}$$

$$\frac{\partial V_D}{\partial t} = (Z_{D,toe} - TWL)\frac{\partial Y_D}{\partial t}, \tag{2}$$

$$\frac{\partial Y_D}{\partial t} = \frac{1}{T_s}(Y_{D,eq} - Y_D), \tag{3}$$

where Y_S represents the position of the shoreline, defined by the mean high water (*MHW*) level located at an elevation of 2.1 m; t is time; Q_L is the gradient in LST rate; x represents the alongshore coordinate; d is the depth of closure (DoC); $Y_{S,eq}$ refers to the cross-shore equilibrium position with K_C defining the erosional and accretional rates; $\frac{q_x}{d}$ represents the alongshore related sediment source; and $\frac{q_y}{d}$ is the cross-shore related sediment source per unit shoreline and unit time. V_D and Y_D represent the eroded foredune volume and the foredune toe position, respectively; $Z_{D,toe}$ is the foredune toe elevation; *TWL* is the total water level; and T_s the response time at which the dune moves to its theoretical equilibrium position $Y_{D,eq}$. Shoreline and

foredune positions are extracted from the onshore end of the shore-normal measured transects presented in Figure 1. Equations (1)–(3) are coupled through Y_D, which modifies $Y_{S,eq}$, that is, the cross-shore component of equation (1) (more details on how the coupling between equations is conducted are given in section 3.2.2). Terms on the right-hand side of equations (1)–(3) are explained in the following sections. The numerical implementation of COCOONED is discussed in Appendix C.

3.2.1. Longshore Transport

Gradients in LST drives beach morphology at temporal scales ranging from hours to centuries and spatial scales ranging from tens of meters to hundreds of kilometers (Ashton et al., 2001; Cowell, Stive, Niedoroda, Swift, et al., 2003; Cowell, Stive, Niedoroda, Vriend, et al., 2003). High-LST gradients can quickly produce large impacts such as inlet closures (Ranasinghe & Pattiaratchi, 1999), rapid build-up of ebb/flood shoals (Oertel, 1972), headland bypassing of large volumes of sand (Kristensen et al., 2016; Storlazzi & Field, 2000), and rotation of pocket beaches and changes in curvature (Harley et al., 2015; Ratliff & Murray, 2014). Persistent alongshore gradients in LST (even small gradients) can result in chronic impacts shaping our coastlines (Antolínez et al., 2018; Ashton et al., 2001, 2002; Ashton & Murray, 2006a, 2006b; Falqués et al., 2017; Idier et al., 2011; Kaergaard & Fredsoe, 2013a, 2013b; Moore et al., 2013; Murray & Ashton, 2013).

LST is modeled in the first term of equation (1) by the alongshore gradient in the LST rate Q_L, where x represents the alongshore coordinate and d is the DoC. We model the DoC according to Hallermeier (1980), but other parameterizations for the active upper shoreface limit, like Birkemeier (1985), Nicholls et al. (1998), Hartman and Kennedy (2016), and Ortiz and Ashton (2016), can be easily incorporated. Q_L is the alongshore transport rate given by

$$Q_L = Q_0 \sin\left(2(\theta_b - \alpha_{shoreline})\right), \tag{4}$$

where Q_0 is obtained applying the CERC sediment transport formula (Komar, 1971),

$$Q_0 = K_L \frac{\rho}{(\rho_s - \rho)p} \frac{H_{S,b}^2 C_{g,b}}{16}, \tag{5}$$

where ρ is the density of water, $H_{S,b}$ is the breaking wave height, $C_{g,b}$ is the group velocity of the wave at breaking, K_L is an adjustable constant derived empirically, ρ_s is the sediment density, and p is the porosity of the sediment. Other formulas such as Kamphuis (1991), Bayram et al. (2007), Mil-Homens et al. (2013), and van Rijn (2014) can also be implemented. As θ_b is the breaking wave direction and $\alpha_{shoreline}$ is the orientation of the coastline, $\theta_b - \alpha_{shoreline}$ represents the relative angle between the waves and the shoreline. The waves at 20-m water depth are obtained with the nearshore propagation model described in section 3.1 and further propagated using linear theory until breaking assuming a relationship $H_{S,b} = 0.45 d_b$, with d_b the breaking depth (see the location of the 20-m contour in Figure 6).

3.2.2. Cross-Shore Transport

Cross-shore sediment transport (CST) processes tend to operate on much shorter timescale than LST. Trends such as seasonal fluctuations (Aubrey, 1979; Blossier et al., 2017; Cohn & Ruggiero, 2016; Davidson et al., 2010; Ruessink et al., 2007; Walstra et al., 2012) or El Niño related phenomena (Barnard et al., 2012, 2017) are easier to predict than storm-induced changes (Callaghan et al., 2013; Coco et al., 2014), even though both have significant impacts on the shoreline and must be included in a complete model. An exception to this generalization is the shoreline change related to long-term sea-level variability, which results in a readjustment of the profile to the new water levels and is a cross-shore response (Bruun, 1962).

CST is modeled in the second term of equation (1) using a modified version of the Miller and Dean (2004) model. The model is based upon the general observation that the shoreline tends to approach an equilibrium position ($Y_{S,eq}$) exponentially with time when subjected to constant forcing

$$Y_{S,eq} = \Delta Y_0 + \Delta Y_{eq}, \tag{6}$$

where ΔY_0 is a baseline condition and ΔY_{eq} is the equilibrium position forced by changes in the local water surface elevation due to a combination of local tide, storm surge, and wave induced setup.

$$\Delta Y_{eq} = W_b^* \frac{WL_{ST}}{B + d_b}, \tag{7}$$

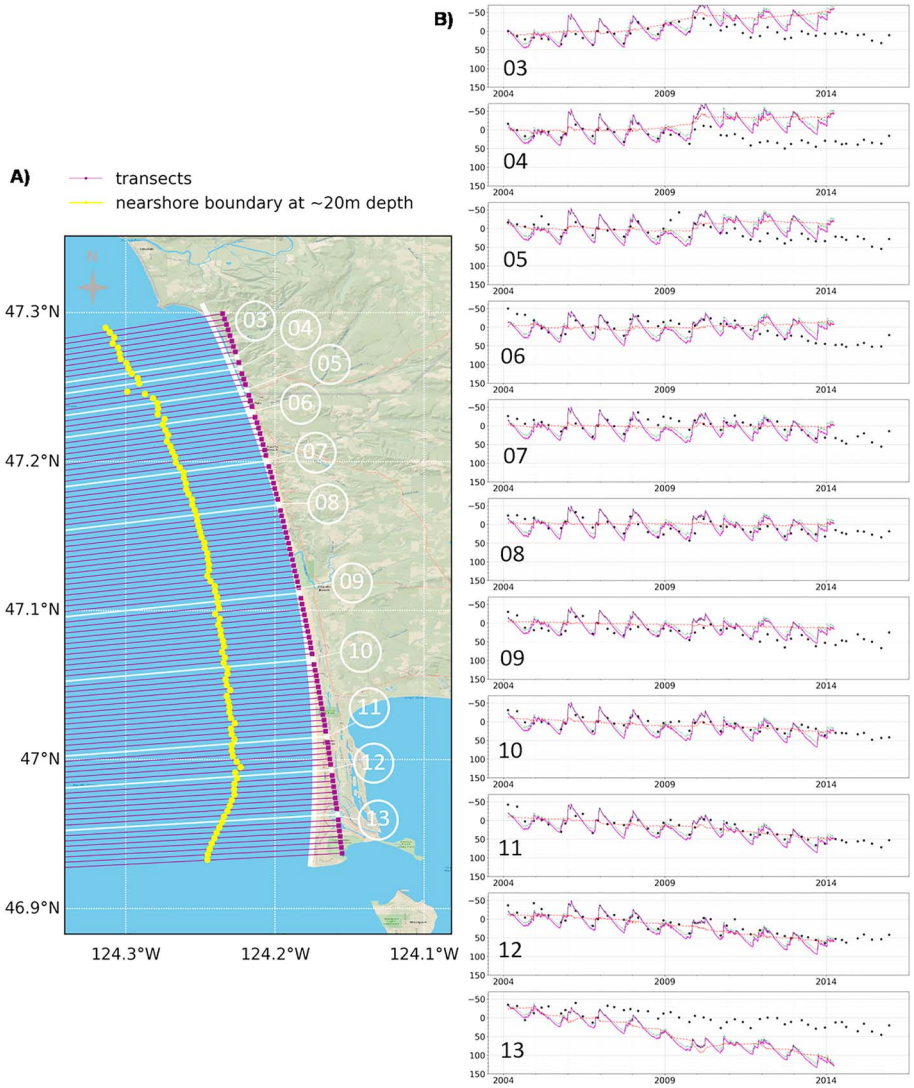

Figure 6. Panel (a) shows the transects used in the numerical model (purple transects), the location of the wave boundary conditions at 20-m depth (yellow dots), and the corresponding transects where observations are available (white). Panel (b) shows the transects from north to south (upper to lower plots), comparing the observations available (black dots) against the modeled shorelines (continuous lines; in purple model runs with cross-shore and longshore terms, in red with only the longshore term). The Y axis is defined in meters and defines the cross-shore position. Zero is the initial shoreline position, positive defines seaward progradation, and negative landward retreat relative to that initial position.

where B is the berm height, d_b the breaking depth (obtained assuming a relationship $H_{S,b} = 0.45d_b$), WL_{ST} is the local water surface elevation driving short term processes,

$$WL_{ST} = 0.106H_{S,b} + SS + AT \tag{8}$$

with $0.106H_{S,b}$ the wave induced setup definition in Miller and Dean (2004), SS the storm surge, and AT the local astronomical tide. W_b^* is the length of the active profile to the breaking point, which is the width of the surf zone. Here we assume an equilibrium "Dean profile,"

$$W_b^* = \left(\frac{d_b}{A}\right)^{3/2}, \tag{9}$$

where A is the beach profile factor also known as the "Dean parameter," which depends on the fall velocity, and therefore on the sediment grain size (e.g. D_{50}) and grain porosity, and is computed according to Dean (1987, 1991).

The CST component of COCOONED contains three adjustable parameters. Two rate "constants" defined by K_C in the second term of equation (1) and representing the accretion rate $K_{C,a}$ and the erosion rate $K_{C,e}$ since these processes act at different timescales and at different speeds. The third parameter defines the baseline condition from which equilibrium shoreline displacements are computed, ΔY_0 in equation (6),

$$\Delta Y_0 = \Delta Y_0{}^* + \Delta Y_{WL_{LT}} + \Delta Y_{LST} + \Delta Y_S + \Delta Y_D, \tag{10}$$

where $\Delta Y_0{}^*$ is the initial baseline location taken during the calibration of the model.

The baseline location is modified through time in order to incorporate long-term adjustments due to long-term water level variations ($\Delta Y_{WL_{LT}}$), like *SLR* or monthly mean sea level anomalies (*MMSLA*) following Bruun (1962).

$$\begin{aligned} \Delta Y_{WL_{LT}} &= WL_{LT}\frac{W^*}{(B+d)}, \\ W^* &= \left(\frac{d}{A(D_{50})}\right)^{3/2}, \\ WL_{LT} &= SLR + MMSLA, \end{aligned} \tag{11}$$

with W^* the total length of the active profile (defined to the DoC d assuming a Dean profile).

The baseline location also accounts for updates in shoreline position from cumulative LST imbalance (ΔY_{LST}), short- to medium-term adjustments due to sediment supply (ΔY_S), and sediment inputs from FDE (ΔY_D),

$$\Delta Y_D = \frac{V_D}{d}. \tag{12}$$

Therefore, by including $\Delta Y_{WL_{LT}}$, an increase in the long-term water level will accelerate the erosion, and a decrease will accelerate progradation; ΔY_{LST} and ΔY_S will adjust the profile baseline from sediment coming in or going out; and ΔY_D will slow down the shoreline erosion rate when FDE happens. Note that ΔY_D through ΔY_0 allows for the coupling between FDE and the shoreline model, that is, equations (1)–(3).

3.2.3. Sediment Supply

Sediment supply can dominate the coastal behavior (Buijsman, Kaminsky, et al., 2003; Buijsman, Sherwood, et al., 2003; Gelfenbaum et al., 1999; Kaminsky et al., 2010). Thus, it is incorporated into the model in the third term on the right hand side of equation (1). $\frac{q_x}{d}$ represents the alongshore related sediment source. $\frac{q_y}{d}$ is the cross-shore-related sediment source per shoreline meter and unit time. q_x incorporates sediment sources entering the system from the south and leaving through the north boundary, and q_y incorporates sediment coming from the lower shoreface. In this work, sediment sources are derived according to the sediment budget proposed by Kaminsky et al. (2001) and Ruggiero, Buijsman, et al. (2010) for NBSC. Note that, for example, with q_x we could simulate the effects of a perpendicular structure trapping sediment by including a volume of sediment per unit time proportional to the wave-related longshore transport and with opposite sign. And with q_y we could mimic shoreline progradation during marine transgression periods (Beets & van der Spek, 2000) if the nearshore sources of sediment are larger enough to overcome the expected recession given by the long-term adjustments due to persistent water level variations determined by the "Bruun Rule"-based equation (11).

3.2.4. FDE Model

FDE is modeled according to Kriebel and Dean (1993) in equations (2) and (3), using the total water level (*TWL*) instead of just storm surge as in Mull and Ruggiero (2014). The volume of sediment eroded by Kriebel and Dean (1993) is derived geometrically. The foredune begins to erode when the *TWL* exceeds the foredune toe elevation ($Z_{D,toe}$). For these two reasons, the sensitivity of the model to the dune toe (and dune crest) elevation is high. Therefore, we try to reduce the uncertainty of these values by extracting them manually from the observed profile data. The model predicts a potential erosion response (Y_D) for a particular storm based on equilibrium profile theory assuming that dunes do not erode instantaneously and that the timescale for an erosion response (T_s in equation (3)) is often greater than a typical storm duration. Therefore, the potential erosion is adjusted by the ratio of the two timescales. The maximum potential foredune retreat distance $Y_{D,eq}$ is predicted by

$$Y_{D,eq} = \frac{\left(TWL - Z_{D,toe}\right)\left(W_b^* - \frac{d_b}{\tan\beta_b}\right)}{Z_{D,crest} - Z_{D,toe} + d_b - \left(TWL - Z_{D,toe}\right)/2}, \tag{13}$$

Table 1
Comparison of GOW Nodes (G) Against Buoys and Validation of the Hybrid Downscaling (D)

					rho			RMS			BIAS		
Buoy	Node	Depth(m)	lon(°)	lat(°)	Hs	Tp	θ	Hs(m)	Tp(s)	θ(°)	Hs(m)	Tp(s)	θ(°)
NDBC_46089	G	2293.3 [∞]	125.771° W	45.925° N	0.95	0.73	0.84	0.42	3.04	27.77	−0.17	0.93	−2.82
NDBC_46029	D	134	124.485° W	46.143° N	0.92	0.72	0.82	0.52	2.93	25.14	−0.11	−0.84	−5.63
NDBC_46041	D	128	124.472° W	47.353° N	0.93	0.72	0.81	0.49	2.95	23.68	−0.12	−0.86	−0.44
NDBC_46211	D	40	124.244° W	46.858° N	0.92	0.72	0.79	0.47	3.07	20.08	−0.14	−0.83	−4.23
NDBC_46243	D	24.4	124.128° W	46.216° N	0.91	0.73	0.77	0.51	3.18	20.76	−0.06	−0.89	−1.71
NDBC_46248	D	182	124.640° W	46.134° N	0.93	0.71	0.81	0.48	3.24	26.58	−0.04	−0.89	−3.05

Note. NDBC = National Data Buoy Center; GOW = Global Ocean Waves; rho = correlation coefficient; RMS = root mean square error; BIAS = bias.

where $TWL = SS + AT + R_2$, with R_2 the 2% exceedance wave runup height (setup plus swash, based on the empirical parameterization of Stockdon et al., 2006). Water level components are defined in section 2.2 and shown in Figure 4.

FDE occurs when TWL exceeds $Z_{D,toe}$ during a storm, and the profile is in the collision regime according to Sallenger (2000) storm impact scale. $\tan\beta_b$ is the backshore beach slope. $Z_{D,toe}$, $Z_{D,crest}$, and $\tan\beta_b$ are obtained from data according to section 2.2 (see Figure 3).

The response time T_s (in hours) is obtained empirically by Kriebel and Dean (1993) with the dimensionless parameter $C_1 = 320$ and g the acceleration of gravity,

$$T_s = \frac{C_1 H_{s,b}^{3/2}}{g^{1/2} A^3}\left(1 + \frac{d_b}{Z_{D,crest} - Z_{D,toe}} + \tan\beta_b \frac{W_b^*}{d_b}\right)^{-1}. \quad (14)$$

The Kriebel and Dean (1993) FDE model assumes that the volume of sediment eroded from the foredune during storms is deposited in the nearshore as a new equilibrium profile is established. Therefore, we incorporate this volume in the profile according to equation (12).

3.2.5. Backshore Slope ($\tan\beta_b$)

According to equations (13) and (14), steeper backshore slopes have a greater erosion potential (as an impact of the TWL formulation) than the same profile with a milder slope. Therefore, we have developed a model to incorporate seasonal variations in the backshore slope ($\tan\beta_b$). Quarterly beach backshore slopes are automatically computed between the 2.1 and 3.6 m (the lowest foredune toe position found is 3.7 m), and grain size distributions are available (Figure 2; more details in section 2.2). We define a seasonal model for the backshore slope ($\tan\beta_b$) according to

$$\tan\beta_b(t) = \gamma_0 + \gamma_1\phi_{50} + \gamma_2\cos\left(\frac{2\pi t}{365}\right) + \gamma_3\sin\left(\frac{2\pi t}{365}\right); t = 1 \ldots 365, \quad (15)$$

where $\phi_{50} = -\log_2 D_{50}/D_0; D_0 = 1mm$. ϕ_{50} represents the median grain size. t is the "day of the year," and γ_0, γ_1, γ_2, and γ_3 are coefficients obtained by multiple regression analysis (MRA). To improve the MRA model (equation 15), we classify the sediment sample distributions collected for each of the 14 profiles in an optimum number of three different groups applying an unsupervised classification algorithm (K-means algorithm), and we fit a MRA model for each of the groups (Figure B1). The aim of this classification is to adapt the MRA model to the different behavior in the seasonal fluctuations detected in the observed slopes (Figure 2). Figure B2 shows that a model accounting for the spatial variations only would underestimate FDE erosion relative to a model that also incorporates seasonal fluctuations in beach slope. Appendix B presents details on the profile classification according to their sediment grain size distribution.

4. Application and Results

We apply COCOONED to the NBSC (section 2.1 and Figure 1) to explore the shoreline response and FDE along 40 km of a coastal sub-cell for 35 years (1979–2014).

First, we perform the nearshore wave propagation (explained in section 3.1 and Appendix A) and compare the results obtained at the locations of several NDBC buoys (Figure 1), and we summarize the comparisons in Table 1.

Table 2
Model Parameters Summary in the Transects With Measures According to Figure 1

	Δx_k (m)	D_{50} (mm)	d (m)	K_L	$K_{C,a}$	$K_{C,e}$	ΔY_0 (m)	B (m)	γ_0	γ_1	γ_2	γ_3	$Z_{D,toe}$ (m)	$Z_{D,crest}$ (m)
02	427.23	0.1438	12.61	0.18	0.00019	0.0225	100.	0.10	−29.3164	38.2623	−1.21899	−10.1878	3.80	5.00
03	427.22	0.1441	12.31	0.18	0.00019	0.0225	100.	0.10	−29.3164	38.2623	−1.21899	−10.1878	3.80	5.00
04	427.31	0.1457	12.33	0.18	0.00019	0.0225	100.	0.10	−29.3164	38.2623	−1.21899	−10.1878	3.80	5.00
05	427.22	0.1503	12.78	0.18	0.00019	0.0225	100.	0.10	−29.3164	38.2623	−1.21899	−10.1878	3.80	4.50
06	427.21	0.1525	13.13	0.18	0.00019	0.0225	100.	0.10	−29.3164	38.2623	−1.21899	−10.1878	4.00	6.00
07	427.18	0.1529	12.57	0.18	0.00019	0.0225	100.	0.10	−29.3164	38.2623	−1.21899	−10.1878	4.00	6.50
08	427.16	0.1464	12.26	0.18	0.00019	0.0225	100.	0.10	−29.3164	38.2623	−1.21899	−10.1878	4.00	5.00
09	427.24	0.1654	12.65	0.18	0.00019	0.0225	100.	0.10	−29.3164	38.2623	−1.21899	−10.1878	4.	6.00
10	427.20	0.1602	12.33	0.18	0.00019	0.0225	100.	0.10	−29.3164	38.2623	−1.21899	−10.1878	4.00	7.50
11	427.21	0.1777	12.32	0.18	0.00019	0.0225	100.	0.10	−29.3164	38.2623	−1.21899	−10.1878	4.00	7.00
12	427.28	0.1995	12.47	0.18	0.00019	0.0225	100.	0.10	26.4846	13.3733	−3.70423	−12.1023	3.70	7.50
13	427.26	0.255	12.16	0.18	0.00019	0.0225	100.	0.10	26.4846	13.3733	−3.70423	−12.1023	4.30	8.00
14	427.14	0.3059	12.14	0.18	0.00019	0.0225	100.	0.10	43.0436	−13.2867	−0.264803	−2.56074	4.50	8.00
15	427.14	0.3059	12.14	0.18	0.00019	0.0225	100.	0.10	43.0436	−13.2867	−0.264803	−2.56074	4.50	8.00

The propagated nearshore waves match well with the wave parameters measured at the buoy locations as did the wave hindcast values used in the offshore boundary condition when looking at the estimators (Table 1). The only concern with the propagated nearshore waves obtained is a small BIAS in wave angles. Since wave direction bias can be problematic when evaluating the shoreline response, we discuss how we address this systematic error in Appendix C. The nearshore propagation developed for this work is efficient, computational inexpensive, and similar to that presented in García-Medina et al. (2013) for the same region.

Then, we use the nearshore waves to drive COCOONED. The numerical implementation of COCOONED is discussed in Appendix C. We define 99 transects with a spatial resolution (distance between transects) $\Delta x_k \simeq 427$ m (Figure 6) and a time step of $\Delta t = 1$ hr. The implicitness parameter chosen is $\Omega = 0$ (forward Euler scheme), which guarantees stability and convergence for the Δx_k and Δt taken. We use 11 years (2004–2014) of seasonal topo-profile surveys (40 dates in total) for training the model coefficients (section 2.2 and right panels in Figure 1). Table 2 summarizes the parameters incorporated in the model. Sediment supply is included as boundary conditions from the integrated sediment budget developed in Kaminsky et al. (2001) with 1.0 Mm^3/year of sand entering the littoral system from the south, 0.1 Mm^3/year of sand exiting to the north, and 0.3 Mm^3/year of cross-shore feeding from the lower shoreface (Kaminsky & Ferland, 2003).

The results obtained during the training process are shown in Figure 6, and three summary statistics (correlation coefficient, root mean square [RMS] error, and bias) are presented in Table 3 for transects 03 to 13. The statistics are computed on a daily basis to match measured data with model predictions (Ruggiero, Buijsman, et al., 2010). The best model skill occurs for transects south of the Copalis River (transects 7–12). North of this location, the inner shelf is covered by only a very thin layer of Holocene sand which complicates the comparison for a one-line model application. Furthermore, in the observed data beach slopes get

Table 3
Model Performance in the Period Measures Are Available

	03	04	05	06	07	08	09	10	11	12	13
rho	0.696	0.251	0.249	0.382	0.593	0.637	0.678	0.749	0.847	0.915	0.819
RMSE (m)	22.837	31.613	25.461	24.169	21.216	16.569	18.457	17.891	16.040	18.245	59.612
BIAS (m)	−12.333	−18.386	−1.685	6.879	13.602	1.443	−9.198	9.907	8.009	13.476	50.724

Note. rho = correlation coefficient; RMS = root mean square error; BIAS = bias.

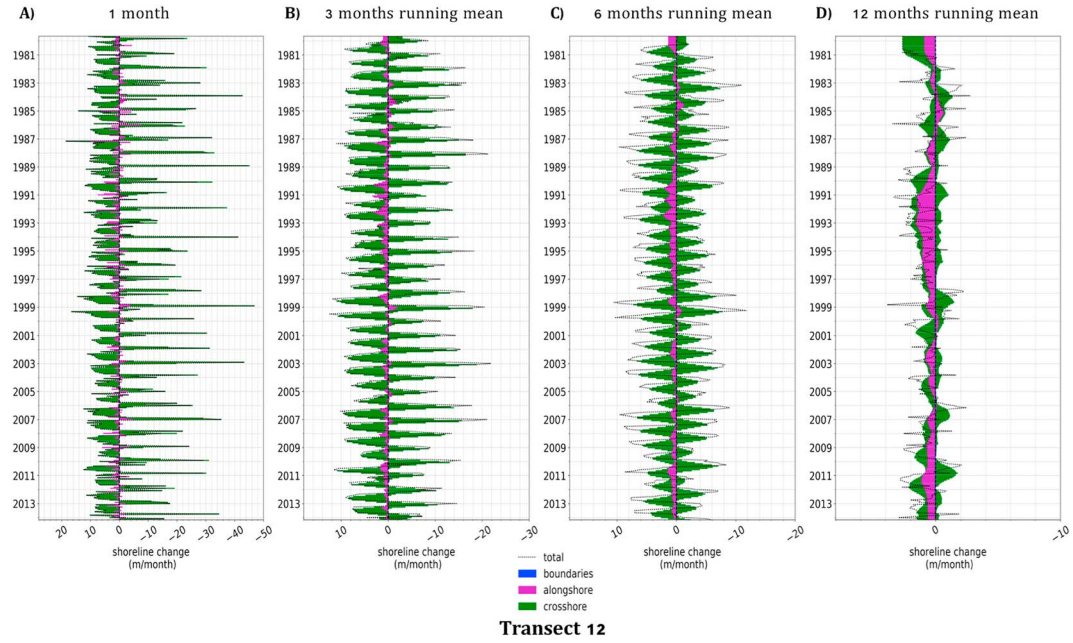

Figure 7. Comparison of the cross and alongshore components of shoreline change (meter per month) over the entire modeled period for a representative transect (transect 12). Panel (a) monthly shoreline change, panel (b) 3 monthly running mean of the shoreline change contributions, panel (c) 6 monthly running mean of the shoreline change, and panel (d) yearly running mean of the shoreline change. The cross-shore component of shoreline change is represented in green, the alongshore component in purple and the total shoreline change with a black line. In panels (b), (c), and (d) the cross-shore and alongshore components show the positive and negative contributions during the aggregated period, and the total shoreline change line represents the net shoreline change. Positive values represent accretion and negative erosion. *Y* axis are scaled according to the temporal aggregation.

shallower and shoreline variability higher toward the north; the reason why, for example, the RMS error is higher in the northern transects. We do not include transects 2, 14, and 15 because they are too close to the boundaries of the model and they are still affected by the imposed sediment supply. Furthermore, they are too near Point Grenville in the north and the Grays Harbor North Jetty in the south for the model predictions to be reliable (due to these being areas experiencing wave sheltering, complex ebb-tidal bathymetry, the presence of tidal currents, sediment bypassing, etc). Transect 13 is also influenced by the northern flank of Grays Harbor ebb-tidal delta (shown in the 20-m contour in Figure 6). COCOONED results are overall fairly consistent with the measured data reproducing the general observed trend of regional shoreline rotation and the seasonal fluctuations (Figure 6).

4.1. Exploring Cross-Shore and Longshore Contributions to Shoreline Change

The 35-year hindcast of hourly shoreline position developed in this paper permits an exploration into the relative contributions of longshore and cross-shore processes to shoreline change at NBSC accounting for the effect of wave action and varying water levels. Alongshore and cross-shore contributions are obtained, respectively, from $\frac{-1}{d}\frac{\partial Q_L}{\partial x} + \frac{-1}{d}q_x$ and $K_C(Y_{S,eq} - Y_S) + \frac{-1}{d}q_y$ terms in equation (1). Figure 7 shows how at "transect 12," cross-shore contributions are predominant at shorter timescales (monthly; Figure 7a) and longshore processes become more relevant at longer timescales (annual; Figure 7d). The influence of interannual variability present in the forcing at monthly, seasonal, and six monthly scales is also apparent in the modeled shoreline change. For example, in December 1998 (e.g., 1998–1999) the monthly erosion rate related with cross-shore processes is above 40 m/month (Figure 7a), more than double of the average winter erosion rate (~15 m/month) inferred from Figure 7b. High erosion rates are usually followed by high accretion rates (1998–1999) but not always (2010–2011). This is exhibited in Figure 7c, which shows the aggregated erosional and accretional behavior in the monthly shoreline change rate due to cross-shore processes. We can see how longshore related erosion/accretion rates appear significant at seasonal scale (due to the seasonal cycle in wave directions); however, longshore transport becomes the most relevant at yearly

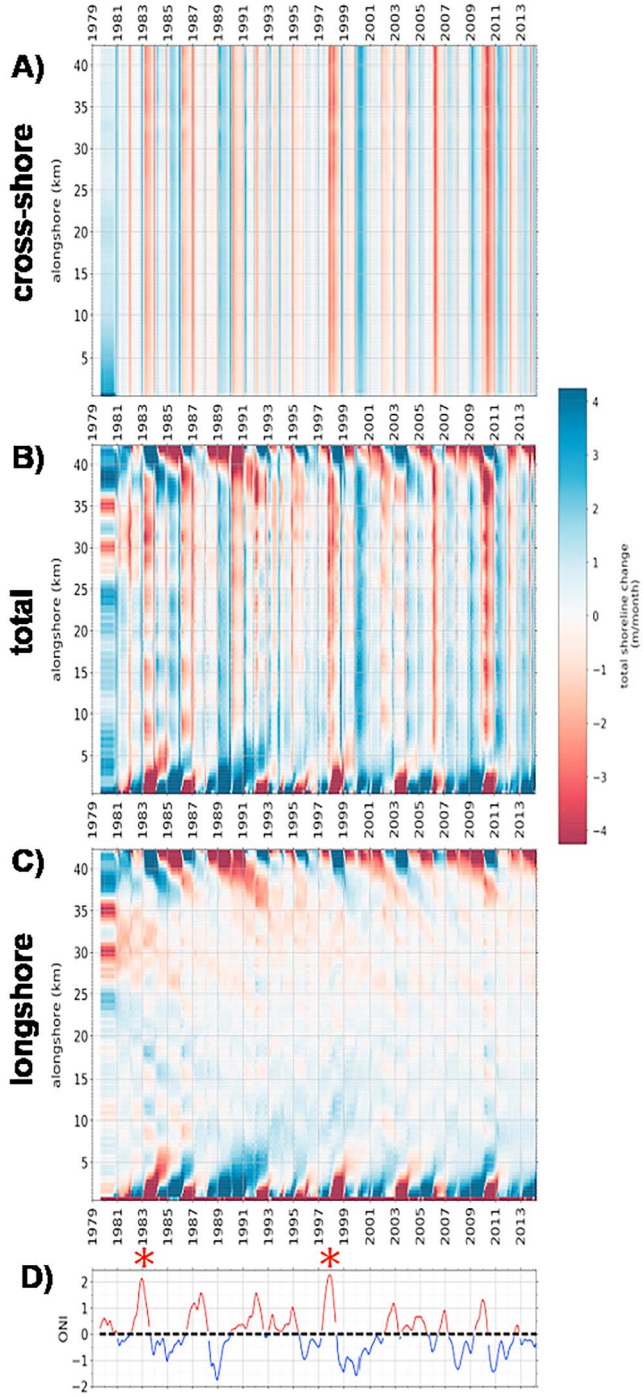

Figure 8. Spatial and temporal monthly net shoreline change rate variability. Panel (a) shows the cross-shore contribution. Panel (c) shows the alongshore contribution. Panel (b) shows the total contribution. The horizontal axis represents time and the vertical axis the alongshore locations (increasing to the north). Panel (d) is the Oceanic Niño index in degree Celsius. Asterisks highlight the major "El Niño" events. Positive in blue refers to accretion and negative in red erosion.

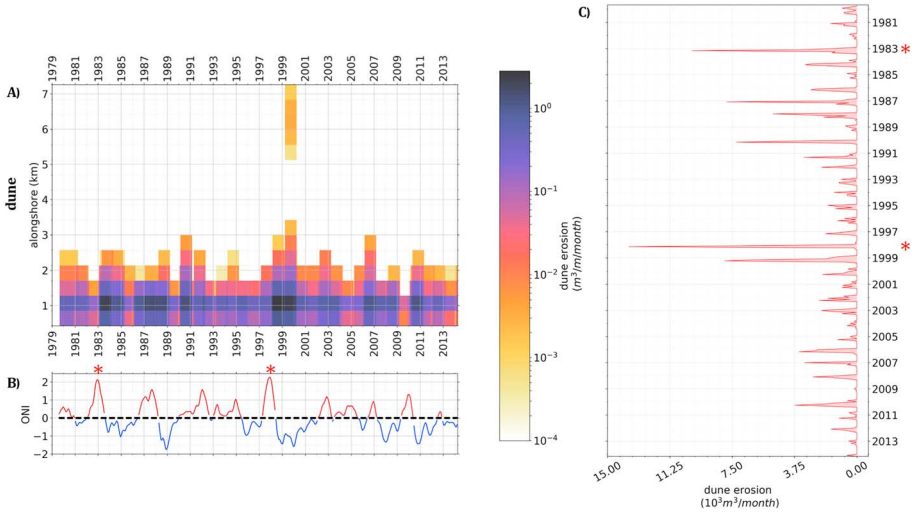

Figure 9. Foredune erosion variability in the southern part of NBSC (Transects 12 to 15). Panel A represents the foredune erosion for the alongshore positions (vertical axis) through time (horizontal axis) and Panel B is the Oceanic Niño index (ONI) in degree Celsius. Panel C summarizes the total monthly foredune erosion through the study period. Asterisk highlight the major "El Niño" events.

scale. In this southern-located transect we can infer from shoreline change rates the accretional trend of the southern part of the beach, but also short periods of sediment loss (e.g., 1984–1986 and 1999–2001).

Figure 8 introduces the modeled monthly shoreline change rates in time (horizontal axis) for every location (vertical axis) at NBSC. This figure exhibits variability at monthly, seasonal, interannual, and multidecadal scale for the longshore and cross-shore-related shoreline change rates (Figures 8a and 8c, respectively) and also the total shoreline change (Figure 8b). We examine the spatial influence, with longshore processes more evident in the northern and southern boundaries, and little spatial variability in the cross-shore response. We present the results with the Oceanic Niño index (Figure 8d). Figure 8 shows high erosion rates and subcell rotation (accretion in the north and erosion in the south) during the 1982, 1986, 1997, 2002, and 2009 El Niño years (reaching ~3 m/month of shoreline change). However, high rate recoveries and shoreline reorientation (northern erosion and southern accretion) are shown during La Niña events (1988, 1998, 2007, and 2010). Patterns of sand wave propagation from the southern tip of the sub-cell to the north and vice versa that persist in time can also be inferred from the shoreline change rates. For instance, La Niña 1988 is seen in the shoreline change rates until 1996–1997 (with rates of shoreline change in the order of 2–3 m/month), confirming that littoral cell rotations are not simply a consequence of sediment movement during individual seasons followed by subsequent reorientation but rather dominated by decadal scale oscillations (Anderson et al., 2018). Note that when we mention, for example, the 1997 El Niño year, we refer to the 1997–1998 El Niño event, which was initiated in 1997.

4.2. Interannual Variability in Potential FDE

FDE only occurs in the southern part of NBSC (transects 12 to 15) where backshore slopes are steep and there is a greater erosion potential when water levels are high. Observations confirm this erosional behavior in the southern transects (Figure 1), while in the northern area backshore erosion rarely occurs. Figure 9c shows the highest monthly FDE volumes are within the winter seasons of 1983 (40,340 m^3), 1998 (50,350 m^3), and 1999 (45,700 m^3), which are "El Niño" years (e.g., volumes for 1998 year are computed from August 1998 to July 1999). Figure 9a defines the erosional foredune volume for every location between transects 12 and 15. The model suggests that the 1980s were characterized by a higher number of exceptional events (mean of 15,450 m^3 and maximum of 40,350 m^3 in the year 1983) of FDE in contrast to the 2000s (mean of 8,840 m^3 and maximum of 22,160 m^3).

5. Summary and Discussion

5.1. Model Limitations

In this paper we present an efficient shoreline evolution model, which combines a hybrid, dynamic, and statistical, nearshore propagation model for offshore waves, taking advantage of data mining and statistical

methods, and a process-driven coastal model, which combines cross-shore and longshore processes. The model is applied during the period 1979–2014 at the NBSC of the CRLC.

The nearshore wave propagation model combines 500 SWAN runs of multivariate wave conditions in the hindcast period, selected with the maximum dissimilarity algorithm, with statistical interpolation techniques (radial basis functions) used to reconstruct the daily continuous time series in the nearshore. Tests reveal that increasing the number of runs does not significantly improve the results. We could increase the complexity of the nearshore wave propagation by forcing spatial wave and wind fields instead of an uniform multivariate wave climate at the offshore boundary to better represent spatial variability in the domain and the effects of local wind wave generation. Additionally, the nearshore wave propagation could improve splitting the directional spectra in swell(s) and wind sea, including also a proper definition of the directional and frequency spreading. Furthermore, temporal changes in bathymetry, if multiple bathymetries were available, could possibly improve the predictions. Finally, the nearshore waves at the 20-m contour are propagated using linear theory to breaking assuming parallel contours to the shoreline orientation (as it is shown in Figure 6 the 20-m contour at NBSC is nearly parallel to the shoreline). The small bias (~4°) present in the predicted wave direction climate requires the initial shoreline to be rectified with a numerically corrected shore baseline (Appendix A).

The coastal evolution model presented combines the interaction of (1) longshore transport gradients and shoreline change due to waves with a one-line approach, (2) cross-shore transport and equilibrium shoreline change due to both waves and varying water levels, (3) FDE, and (4) the inclusion of profile adjustment via sediment supply. COCOONED accounts for the combined effects of waves and varying water levels in shoreline evolution and FDE covering a wide range of space and timescales, including sequencing and clustering of storm events, and seasonal, interannual, and decadal oscillations of various sorts. The coastal model does omit, however, several processes contributing to changes in natural environments.

We do not consider local variations in wave conditions arising from complicated nearshore bathymetry, so areas close to jetties or headlands are not reproduced as well as the nearby beach to the flank of the ebb-tidal shoal. Coastline accretion or erosion occur in the uppermost portion of the shoreface profile, and the accretion or erosion is distributed across the whole shoreface all at once in this model. This simplified approach neglects delays in propagating the accretion or erosion to the lower parts of the shoreface profile (Kinsela & Cowell, 2015), which over the timescales of decades can alter the rates of coastline response. COCOONED also neglects the effect of seasonal sandbar welding to the upper shoreface profile (Cohn & Ruggiero, 2016), which can complicate the comparisons in shoreline position. Similarly, berms usually build seasonally, and we fix the berm profile to be constant during the simulations. Strong storms can transport sediment from the beach and upper shoreface landward. Such "overwash" events remove sand from the beach and shoreface, inducing shoreline erosion and foredune growth (Cohn et al., 2018). Our foredune model only accounts for erosion; therefore, full recovery over the summer is enforced. Thus, we limit the results to be interpreted as potential FDE, and foredune heights or positions are not updated. For the overtopping regime, which happens when the *TWL* exceeds the foredune crest elevation, our model would assume the maximum *TWL* would equal the foredune crest elevation. Even though the severity of landward transport is ultimately a function of overtopping volume (Cox & Machemehl, 1986) and other parameterizations might be implemented such as the solution given by Rosati et al. (2013). We simply model FDE driven by waves and water levels, foredune recovery is not modeled as the influences of other processes such as the effects of aeolian processes and vegetation interactions complicates the analysis. Backshore slopes, highly influencing FDE (section 3.2.5, Appendix B, and Figure B2), are modeled based on spatial variations on the grain size and temporally reproducing seasonal fluctuations, although other temporal scales (interannual or multidecadal) are not accounted due to the limit in the number of samples available for this study, the backshore slope model presented in section 3.2.5 is flexible to be adapted to local requirements. Finally, sediment sources are forced throughout the south and north boundaries at constant rates, when sediment fluxes from rivers (minor in this study site) are usually discontinuous in time potentially affecting the timescale and quantity the sediment enters into the system. The discretization of the model is based on normal-oriented transects, which could overlap at some offshore location if the evolving shoreline developed strong curvature, although this is not the case in this study. Adapting the numerical scheme presented in Appendix C from transect based—the shoreline position moves "on rails" normal to a reference shoreline—into a 2-D planview grid

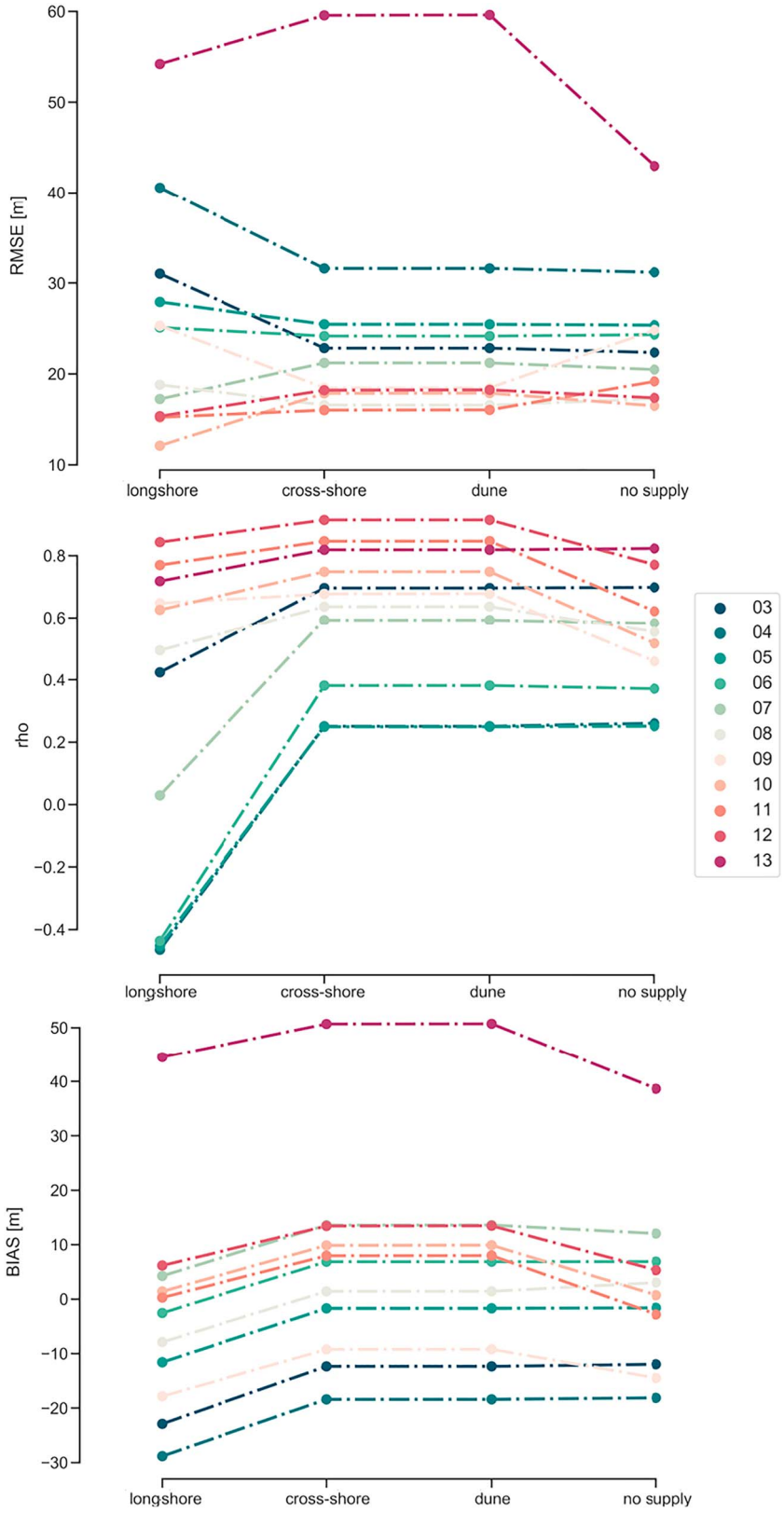

Figure 10. Model sensitivity to longshore, cross-shore, dune erosion, and sediment supply at each transect. The *x*-axis name refers to a new cumulative process in addition to the previous ones. The initial model is run only with the longshore component and sediment supply. rho is the correlation coefficient, RMS is the root mean square error, and BIAS is the bias.

where each cell is filled with a fractional amount of sediment following Ashton et al. (2001); Ashton and Murray (2006a); Robinet et al. (2018) is still possible.

We use seasonal topographic profile surveys in the period 2004–2014 for calibrating the three rate model constants (K_L adjustable aLST rate; erosion $K_{C,a}$ and accretion $K_{C,e}$ rates of the cross-shore model) and the initial baseline position (ΔY_0^*) for the cross-shore term in equation (1). These parameters are those that better reproduce the trend and variability found in the observed data after running the model with a subset of combinations—suggested in previous studies. We do not change the rate constants along the beach during the simulation when profiles with different grain size characteristics could behave differently and changing these rates could also help to mimic the effects that better reproduce the shoreline evolution north of Copalis River. We compute longshore transport with the most widely used formula, the CERC equation (Komar, 1971), which is based on the principle that the longshore transport (including bed and suspended load) is proportional to longshore wave power per unit of length of beach neglecting the direct influence of particle size and beach slope being only valid for sandy conditions. The use of other formulas such as Kamphuis (1991) would allow to account implicitly for the effects of particle diameter and bed slope.

5.2. Sensitivity of Model Components and Calibration Parameters

The shoreline data set presented here is computed with COCOONED accounting for longshore and cross-shore processes, dune erosion, and sediment supply (section 4). As an exploratory exercise we run the model in the period with observations, adding terms sequentially to better understand the contributions of each term in shoreline position. We input the same calibration parameters as presented in Table 2. Figure 10 presents three summary statistics (correlation coefficient, RMS error, and bias) for each transect. The initial computation consists of COCOONED run in one-line mode (longshore) including sediment supply. In the second run (cross-shore) we include the cross-shore term to the longshore and the sediment supply. The effect is a significant improvement in the three statistics. Note that the color map is defined diverging from "transects 7–8," with red colors toward the south and green colors toward the north. This is intended to highlight the difference found in behavior northern and southern Copalis River (section 4). The third run also incorporates dune erosion, as shown in section 4.2 sediment supply from dune erosion is not significant in comparison with the imposed sediment supply. Thus, changes in the metrics presented are minimal. The last run does not account for sediment supply during the computations. The lack of sediment supply produces a remarkable reduction in the correlation coefficient and increase in the RMS error in the southern transects (red color map) and a reduction in the bias in the same area. This reduction in the bias together with the reduction in the correlation coefficient responds to a shoreline reorientation opposite to that found in the observed period (2004–2014). This effect is better seen in the southern transects (red color map) compared to the northern transects (green color map).

The model fitting—or parameter training—is performed by exhaustive or hyper-parameter/grid search. Hence, model parameters are set prior to the commencement of the simulation process. In contrast, automated techniques (e.g., Kalman filter, simulated annealing, and particle swan optimization) can discover parameters and their values on their own, based on the training data, with the risk of overfitting the model parameters to better reproduce the training data set. However, exhaustive grid search is not exempt of overfitting if the proposed research guidelines are based in a poorly designed strategy. The strategy followed in this work to avoid overfitting consisted of a physically sensed series of tests isolating the model components (similar to the comparisons shown in Figure 10) and exploring the shoreline responses (time and spatial scales) for different order of magnitudes of the parameter values (Table 2). We present in Table 4 predictions in the observation period (2004–2014) for 13 different tests. Test *selected* is the model we chose that better reproduced NBSC behavior (Section 4). Tests $alon_{1,2,3,4}$ show the sensitivity of the longshore transport constant rate, K_L, by testing values 10% higher and lesser, double, and 1 order of magnitude lesser. Results are not very sensitive to small changes in the K_L ($alon_1$ and $alon_2$), but when moving to much higher values ($alon_3$) or lower ($alon_4$), the model cannot reproduce the timescale of the alongshore processes in NBSC. Tests $cross_{1,2,3,4,5,6}$, are set up with the same criteria, 10% higher and lesser (1 and 2), two test (3 and 4) making double and half $K_{C,e}$ and $K_{C,a}$, and another two tests (5 and 6) with increased and decreased parameters 1 order of magnitude. In general, the two tests with similar values (1 and 2) present similar accuracy, but the other four tests perform worse than the selected parameterization. Test *aloncross* is a combination of increasing the K_L, and decreasing $K_{C,e}$ and $K_{C,a}$ a 10%, and as shown when changing the parameters independently, the results are very similar to the selected parameterization. Finally, test $supply_1$ does not include sediment supply in the model simulation to look at the influence of this "forced" loading of sediment in

Table 4
Comprehensive Model Tests and Sensitivity of the Model Results to Parameters in Terms of Correlation Coefficient (rho) and RMSE

	B (m)	K_L	$K_{C,e}$	$K_{C,a}$	Alongshore	Cross-shore	Dune	Supply
Selected	0.1	0.18	0.0225	0.00019	1	1	1	1
Test $alon_1$	0.1	0.20	0.0225	0.00019	1	1	1	1
Test $alon_2$	0.1	0.16	0.0225	0.00019	1	1	1	1
Test $alon_3$	0.1	0.36	0.0225	0.00019	1	1	1	1
Test $alon_4$	0.1	0.03	0.0225	0.00019	1	1	1	1
Test $cros_1$	0.1	0.18	0.0245	0.00021	1	1	1	1
Test $cros_2$	0.1	0.18	0.0202	0.00017	1	1	1	1
Test $cros_3$	0.1	0.18	0.0450	0.00038	1	1	1	1
Test $cros_4$	0.1	0.18	0.01125	0.000095	1	1	1	1
Test $cros_5$	0.1	0.18	0.00225	0.000019	1	1	1	1
Test $cros_6$	0.1	0.18	0.2250	0.00190	1	1	1	1
Test aloncross	0.1	0.20	0.0202	0.00017	1	1	1	1
Test supply	0.1	0.18	0.0225	0.00019	1	1	1	0

Metric						rho					
Transect	03	04	05	06	07	08	09	10	11	12	13
Selected	0.696	0.251	0.249	0.382	0.593	0.637	0.678	0.749	0.847	0.915	0.819
Test $alon_1$	0.711	0.231	0.242	0.385	0.599	0.638	0.629	0.700	0.824	0.907	0.804
Test $alon_2$	0.687	0.327	0.306	0.419	0.605	0.614	0.629	0.708	0.821	0.905	0.825
Test $alon_3$	0.713	−0.002	0.088	0.262	0.556	0.684	0.609	0.686	0.815	0.902	0.713
Test $alon_4$	0.491	0.708	0.509	0.498	0.600	0.577	0.565	0.679	0.778	0.885	0.826
Test $cros_1$	0.701	0.286	0.282	0.400	0.605	0.611	0.613	0.685	0.811	0.901	0.816
Test $cros_2$	0.698	0.262	0.258	0.403	0.597	0.645	0.650	0.724	0.835	0.911	0.813
Test $cros_3$	0.663	0.297	0.302	0.375	0.563	0.522	0.519	0.572	0.737	0.866	0.803
Test $cros_4$	0.647	0.136	0.132	0.385	0.520	0.701	0.740	0.788	0.865	0.910	0.790
Test $cros_5$	0.508	−0.253	−0.191	0.212	0.406	0.582	0.803	0.738	0.818	0.859	0.739
Test $cros_6$	0.496	0.205	0.272	0.335	0.470	0.448	0.415	0.434	0.658	0.835	0.747
Test aloncross	0.707	0.215	0.226	0.385	0.593	0.657	0.649	0.720	0.835	0.911	0.802
Test supply	0.698	0.261	0.251	0.371	0.583	0.554	0.459	0.517	0.622	0.771	0.823

Metric						RMSE (m)					
Transect	03	04	05	06	07	08	09	10	11	12	13
Selected	22.837	31.613	25.461	24.169	21.216	16.569	18.457	17.891	16.040	18.245	59.612
Test $alon_1$	24.497	33.308	25.951	24.243	21.394	16.474	19.959	16.030	16.641	22.159	63.919
Test $alon_2$	19.925	28.070	23.988	23.809	20.896	16.677	19.931	16.003	15.800	19.921	57.393
Test $alon_3$	45.362	53.388	35.233	27.351	21.714	15.756	20.348	17.134	22.263	34.702	84.070
Test $alon_4$	19.900	14.834	20.205	22.639	19.553	17.127	21.857	15.208	15.164	14.595	43.381
Test $cros_1$	21.780	30.157	25.237	24.940	22.435	17.717	19.917	17.472	17.400	22.297	61.707
Test $cros_2$	22.479	31.299	24.733	23.100	19.921	15.403	20.057	14.431	14.936	19.636	59.713
Test $cros_3$	22.606	28.936	28.345	30.749	29.771	24.769	22.201	25.617	24.351	29.060	66.918
Test $cros_4$	25.011	34.130	25.151	20.974	16.943	13.102	21.494	9.790	12.015	16.052	56.602
Test $cros_5$	26.895	36.253	25.316	21.646	16.324	16.145	23.818	10.715	13.821	17.137	56.301
Test $cros_6$	31.032	37.972	30.618	29.954	27.148	25.789	29.118	27.574	25.692	25.605	64.182
Test aloncross	25.032	33.982	25.830	23.371	20.138	15.271	20.086	14.455	15.362	20.798	62.922
Test supply	22.356	31.189	25.366	24.318	20.479	17.274	24.844	16.484	19.179	17.361	42.964

Note. RMSE = root mean square error.

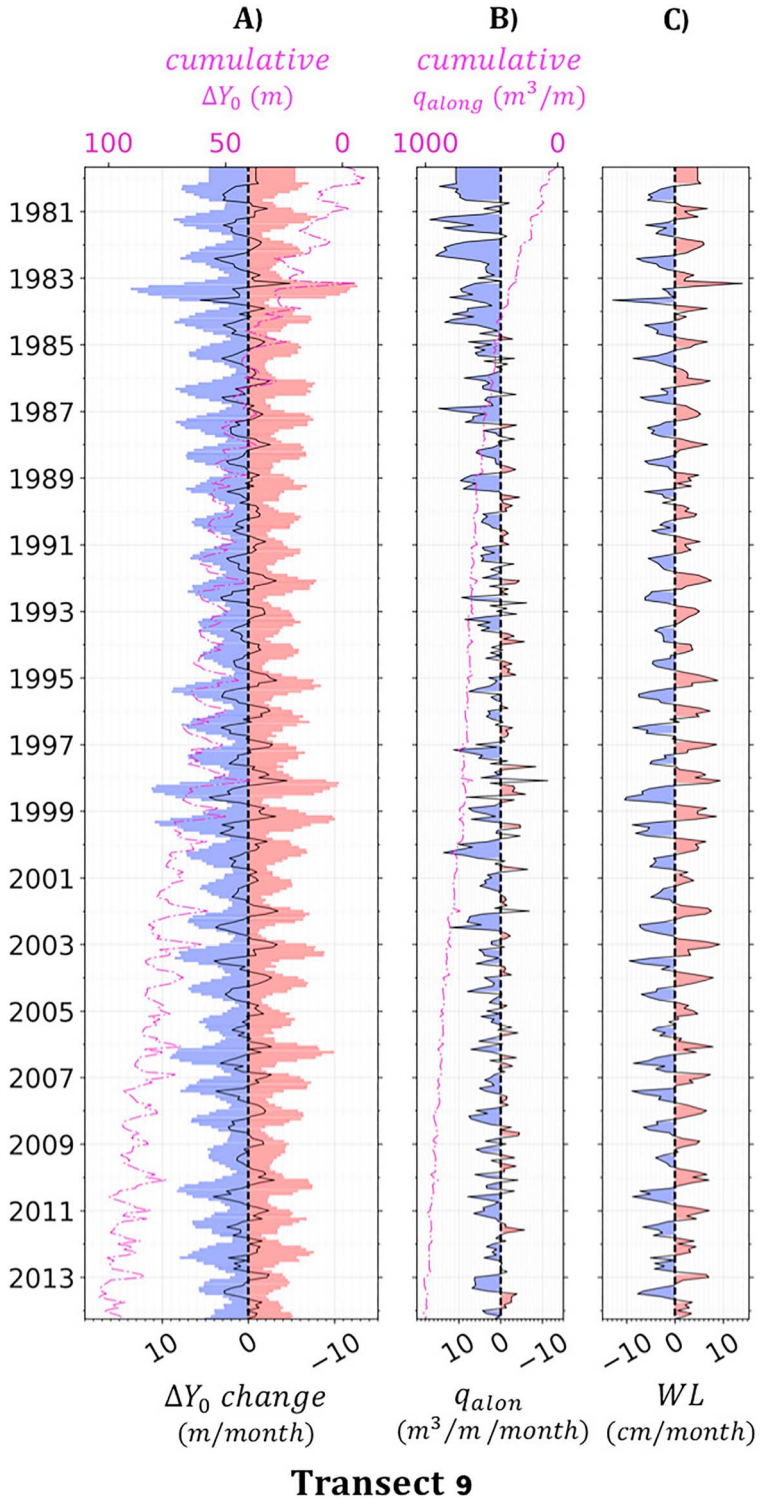

Figure 11. Correlation between ΔY_0, alongshore sediment transport gradients (q_{alon}), and water level variations (WL) in transect 9. Panel (a) represents ΔY_0 (meter per month) parameter change; the black line is the total, the blue is the sum of positive contributions, and negative contributions are plotted in red. The purple line represents the cumulative change in ΔY_0 (m). In panel (b) the negative alongshore sediment transport contribution q_{alon} (cubic meter per meter per month) is plotted in red and the positive in blue. The purple line is the cumulative alongshore sediment transport gradient $cumulative q_{alon}$ (meter per cubic meter). Panel (c) represents the monthly variations in the water level WL (centimeter per month). Cumulative change axis are at the top.

the shoreline evolution. Results show that this is a relevant process that needs to be incorporated. An interesting finding is the different sensitivity to parameters in the northern and southern transects, suggesting that spatial varying constant rates could improve the results. For this, an automated method for selecting the model parameters and cross-validation to avoid overfitting (or low predictability of the model) should be implemented.

5.3. Integrating Long-Term Processes Into Cross-Shore Response Rates

One of the main characteristics in this shoreline model is the adaptation of the cross-shore baseline through the term ΔY_0 as shown in equation (6) and disaggregated in equation (10) into (1) long-term adjustments due to persistent water level variations ($\Delta Y_{WL_{LT}}$), like *SLR* or monthly mean sea level anomaly (*MMSLA*); (2) updates in shoreline position from a cumulative LST imbalance (ΔY_{LST}) or (3) short- to medium-term adjustments due to sediment supply (ΔY_S); and (4) sediment inputs from FDE (ΔY_D). Figure 11 explores the correlation between changes in (1) and (2) and changes found in ΔY_0 for transect 9. The trend in the cumulative LST imbalance (gradients); the remaining sediment in that transect due to alongshore transport (cumulative sediment transport gradient, purple line in Figure 11b) matches the trend present in the cumulative ΔY_0 (purple line in Figure 11a) with a correlation coefficient of 0.996. The monthly water level variations in Figure 11c is correlated with the seasonal component of ΔY_0 (purple line in Figure 11a) with a coefficient of −0.95. Note that the negative correlation occurs as an increase in the water level produces a retreat in the baseline position.

ΔY_0 modifies the rate at which the shoreline change happens. Therefore, an increase/decrease in $\Delta Y_{WL_{LT}}$ will accelerate erosion/progradation rates because of the increasing/decreasing long-term water levels. Variations in ΔY_{LST} and ΔY_S will adjust the profile baseline from sediment coming in or going out, and ΔY_D will slow down shoreline erosion rate after FDE occurs (section 3.2.2). Each of these new features is available, in comparison with Vitousek, Barnard, Limber, Erikson, et al. (2017), thanks to the inclusion of water level variations at several timescales, a different cross-shore approach, and a FDE model.

5.4. Unraveling Shoreline Response Due to Climate Variability and Associated Implications in a Changing Climate

COCOONED delivers 35 years of hourly shoreline hindcast data, derived from 11 years of observed seasonal data (40 surveys). It also extends the data collected at 14 transects over 40 km of beach into gradually and homogeneously distributed transects along the beach. The combination of the different processes and factors contributing to shoreline change allows for meaningful forecasts or hindcasts of raw shoreline change patterns, including the magnitude of rates and their alongshore variations. While this model is not able to exactly mimic the shoreline changes and reproduce what causes the observed temporal and spatial variability in shoreline change rates completely, as an "exploratory" model it can help to unravel the components of shoreline change arising from wave-climate and water-level changes.

For this analysis, we use principal component analysis to decompose the modeled shoreline position variability into empirical orthogonal functions (EOFs). Following Miller & Dean (2007a, 2007b), we use EOF analysis as a statistical method capable of identifying the underlying patterns of cross-shore and alongshore variability modes within the shoreline change. Figure 12 shows the first three EOFs (middle panels) obtained with their corresponding temporal variability (PCs, left panels). The first mode "EOF-1" (Figure 12a) reproduces the 78.20% of the variability in the signal, and it represents the clockwise reorientation trend found in the data. EOF-1 represents the clear break in shoreline change trend at the Copalis River, with higher rates of shoreline progradation to the south of the river than in the north (Ruggiero et al., 2013). The progradation is due to sediment supply entering and being diffused in the system; thus, over the "quasi-linear" trend shown by PC-1, we can appreciate variations related with alongshore transport temporal variability. EOF-2 (Figure 12b) explains the 9.96% of the variability and constitutes the well-known breathing (advance/retreat) behavior in the cross-shore component (Ratliff & Murray, 2014), but it also shows a small rotation effect. As detected by Harley et al. (2011), varying cross-shore processes in the alongshore direction results as a rotation of the shoreline, which is correlated with the alongshore wave energy variability. The temporal variability shown in PC-2 responds mainly to the seasonal cycle, although interannual and multidecadal variability is also found. The third mode EOF-3 (Figure 12c) explains the 8.59% of the variability and defines the rotation mode due to alongshore processes. PC-3 is difficult to interpret due to the nonstationary multiannual and multidecadal variability in the signal.

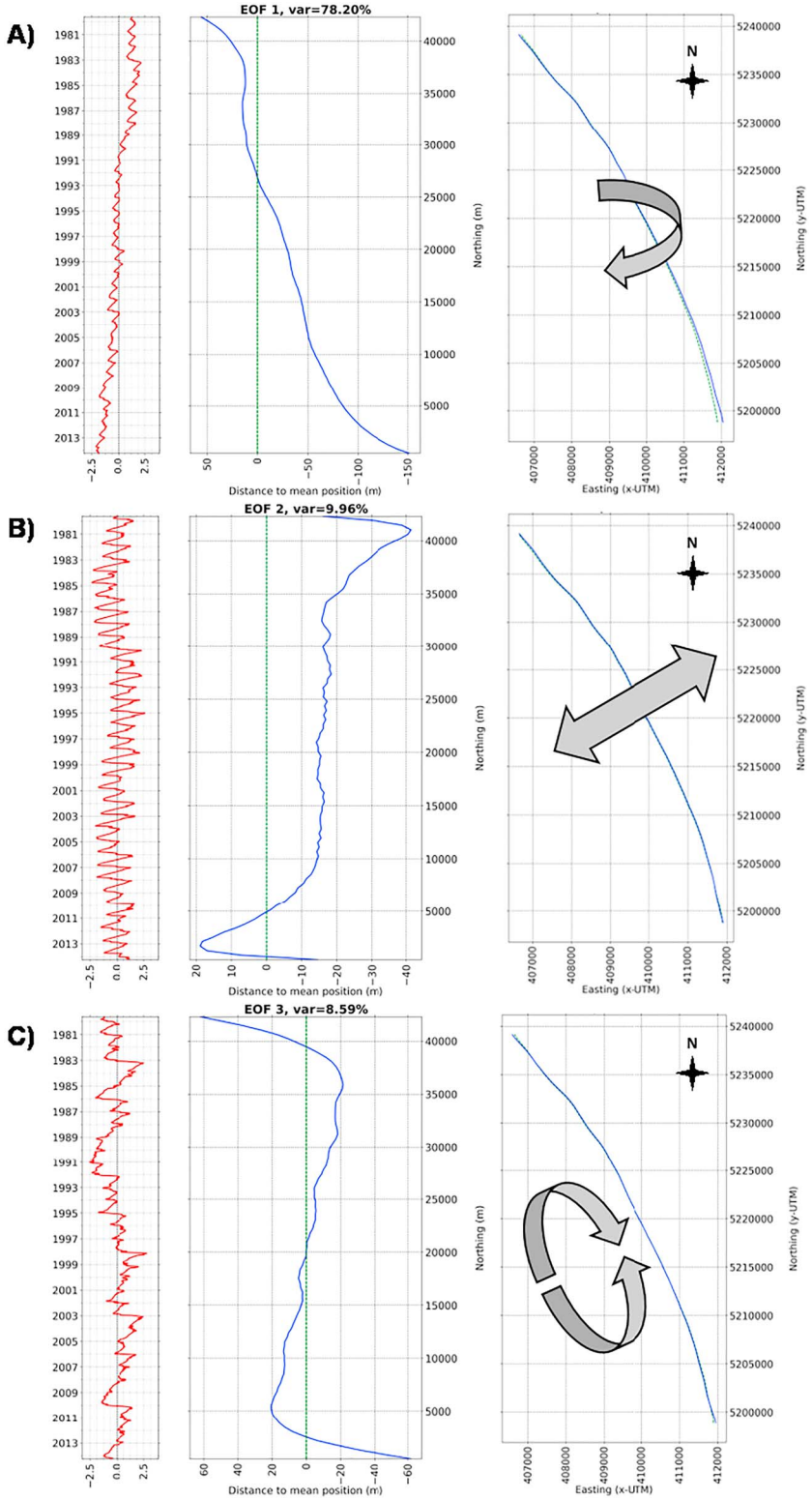

Figure 12. Principal component analysis of the absolute shoreline position. Red lines in the left panels are the temporal indices or principal components. The middle panels represent the spatial modes (empirical orthogonal function [EOF]) relative to the mean shoreline position during the studied period (in green). The *y* axis represents the alongshore direction, and the *x* axis the cross-shore direction. The right panels are sketches of the physical meaning of these spatial modes where the gray arrows try to explain the shoreline behavior (reorientation, breathing, and rotation) in projected coordinates. The first mode (panel a) represents a clockwise reorientation trend. The second mode (panel b) represents the cross-shore variations. The third mode (panel c) represents the rotational variations due to alongshore transport).

6. Conclusion

We have developed an efficient coastal response model (COCOONED) providing a framework that combines a fast delivery hybrid nearshore propagation of offshore waves using SWAN, data mining, and statistical methods, and a process-driven coastal evolution model. COCOONED combines longshore transport due to waves, cross-shore transport due to waves and varying water levels, a FDE model, and the inclusion of profile adjustment by sediment supply, covering a wide range of spatial and temporal scales, including sequencing and clustering of storm events, and seasonal, interannual, and multidecadal oscillations. We also model the influence of FDE on shoreline erosion rates as well as the influence of sediment supply. The numerical implementation of COCOONED allows for the application of input reduction and acceleration techniques for accurately reducing the computational effort taking advantage of the "Standard $\Omega-$*scheme*" implemented and the Jacobian Free Newton Krylov method used for solving the equations. COCOONED is applied in the NBSC of the CRLC (Washington, USA) and extends 11 years of seasonal data (40 surveys) into an hourly shoreline hindcast for 35 years. It also extends the data collected at 14 transects in 40 km of beach into gradually and homogeneously distributed transects along the complete beach. With the modeled shoreline position data set, an EOF analysis identifies three main behavioral modes in NBSC: a clockwise reorientation trend in shoreline, a breathing mode related with cross-shore processes, and a rotational mode related with alongshore processes, unraveling seasonal, interannual, and multidecadal shoreline variability. COCOONED is ready to address coastal responses to projected future climate change in a probabilistic framework accounting for uncertainties in global climate models.

Appendix A: Hybrid Propagation of Nearshore Wave Conditions

We apply the maximum dissimilarity algorithm following Camus et al. (2011) to the hourly offshore multivariate time series of $H_{S,0}$, $T_{P,0}$, and θ_0. After several increases in the size of the subset we found an optimum number of $M = 500$ hourly sea states to propagate numerically.

We perform stationary offshore-to-nearshore/deep-to-shallow water wave transformation of the most representative hourly sea states selected above using the SWAN model (Booij et al., 1999) in cartesian coordinates. We define two nested structured and regular grids spanning the complete Washington State coast. The first grid covers the shelf at a resolution of 1 km, with the second being a coastal grid at 200-m resolution. Both grids are oriented north to south. The offshore boundary condition of the numerical grid matches the depth at which we take waves from GOW2 hindcast in deep water (the edge of the continental shelf). The bathymetry used in the computational domain comes from National Oceanic and Atmospheric Administration Tsunami 1/3 arc-second NAVD 88 Digital Elevation Model (Carignan et al., 2009). We define the boundary conditions using constant JONSWAP spectrum along the offshore border of the grid characterized by hourly $H_{S,0}$, $T_{P,0}$, and θ_0, with a peak enhancement parameter $\gamma = 3.3$ and a directional width expressed in terms of the power of the cosine $m = 4$. We run stationary SWAN computations, although it implies instantaneous wave propagation across the domain.

Finally, we carry out the reconstruction of hourly nearshore wave parameters (H_S, T_M, T_P, and θ) during the period 1979 to 2014 with a spatial resolution of 200 m by an interpolation technique based on radial basis functions. Radial basis functions are a scheme that is very convenient for scattered and multivariate data (Franke, 1982). The aim of the radial basis functions application is the evaluation of the interpolation function of the propagated significant wave height RBF_H, the evaluation of the interpolation function of the propagated peak period RBF_T, and the evaluation of the interpolation function of the components x and y of the mean wave direction $RBF_{\theta x}$ and $RBF_{\theta y}$, respectively. Here we use Gaussian functions as basis functions, we implement Euclidean-circular distances, and we use Rippa (1999) algorithm for the estimation of the optimal shape parameter. Further details of this nonlinear multivariate interpolation technique implementation are given in Camus et al. (2011).

Appendix B: Multivariate Classification of the Sediment Grain Size Distributions

To improve the MRA (equation (15)), we apply the K-means algorithm (implemented in the Scikit-learn library for Python 2.7; Pedregosa et al., 2011) to the sample distributions collected for each of the 14 profiles, and we obtain an optimum number of three different groups. This classification improves the MRA model

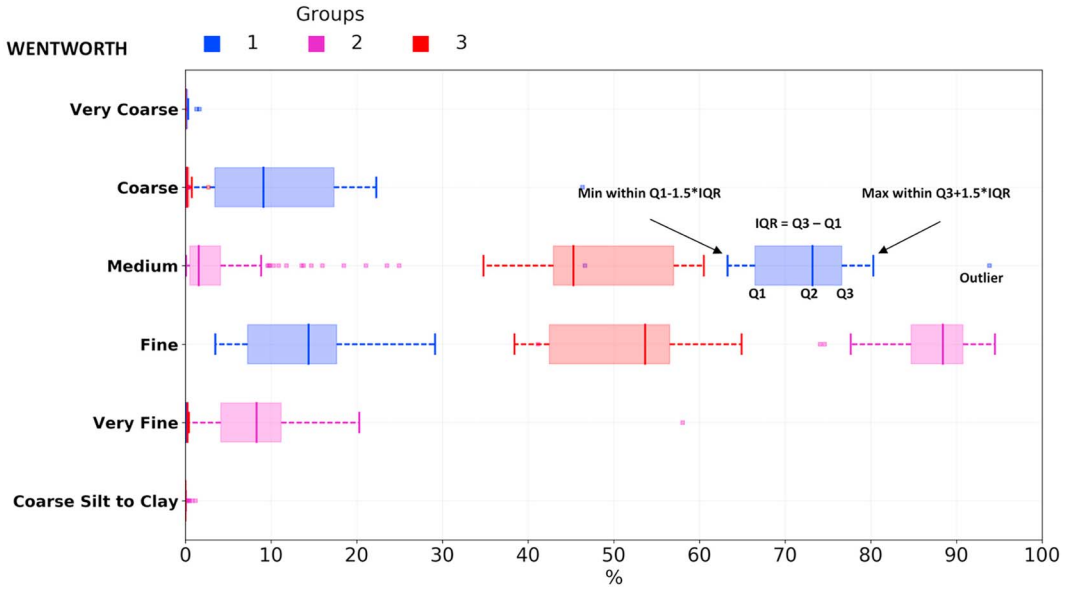

Figure B1. Unsupervised clustering (*K*-means technique) of the grain size distributions (defined by the relative weight of particles in the sample found into each of the Wentworth grain size classes) available for each transect location in the period 1997–2004. The colors represent each of the three groups defined. Each group distribution is characterized using box plots for the Wentworth classes. Each box is defined by the lower quartile (*Q*1, the value below there is a 25% of the data, representing the median of the first half of the values) and the upper quartile (*Q*3, the value below there is a 75% of the data, representing the median of the second half of the values). The second quartile or median (*Q*2) is indicated within a strip into the box. The interquartile rank (*IQR*) is defined by the difference between the third quartile, *Q*3, and the first quartile, *Q*1, and it helps to measure the variability. The box is extended with lines extending horizontally from the boxes (whiskers) until the lowest datum still within 1.5 times the *IQR* of the lower quartile for the left line, and the highest datum still within 1.5 times the *IQR* of the upper quartile for the right line. Any data not included between the whiskers are considered an outlier.

by fitting equation (15) for each of the groups. The multivariate classification accounts for each of the relative weight particles in the sample distribution according to the Wentworth grain size classes (Wentworth, 1922): coarse silt to clay (<0.0625 mm), very fine sand (0.0625–0.125 mm), fine sand (0.125–0.25 mm), medium sand (0.25–0.5 mm), coarse sand (0.5–1.0 mm), and very coarse sand (1.0–2.0 mm). Each group distribution is characterized using box plots for the Wentworth classes (see Figure B1). Box plots help us to look at how the samples are distributed into each of the groups and define the optimum number of clusters. Group 1 (blue) contains a high presence of medium sand (67% to 78%) and relative low amounts of fine sand (5% to 15%) although there are anomalous samples showing values of 30% of fine sand. Group 1 is the only group with the presence of coarse sand (5% to 20%) and a rare presence of very coarse sand (<5%). It is representative

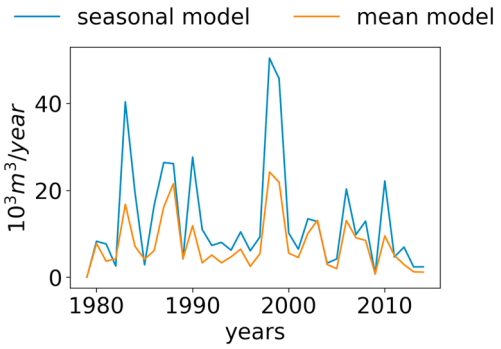

Figure B2. Total annual dune erosion computed from August to July. The orange line shows the dune erosion computed with a backshore slope model for each transect group fitted with a mean mode dependent on the grain size (γ_0 and γ_1). The blue line shows the dune erosion computed with a backshore slope model for each transect group including a mean mode (γ_0 and γ_1) and seasonal fluctuations (γ_2 and γ_3).

of the southern profiles (transects 14 and 15) near the mouth of Grays Harbor, with the steepest slopes (horizontal:vertical—$H{:}V \simeq 25$; Figure 2). Group 2 (purple) contains very high amounts of fine sand (85% to 91%), very low amounts of medium sand (<5%), a significant amount of very fine sand (5% to 11%), and even some silt to clay. Group 2 is representative of the northern area of the beach (transects 2 to 11) with the mildest slopes ($50 \leq H{:}V \leq 150$, Figure 2). Group 3 is a transitional group between 1 and 2, which contains very high amounts of medium and fine sand (42% to 56%) and rarely coarse or very fine sand. Group 3 is representative of transects 12 and 13 with slopes $H{:}V \simeq 50$. We train the set of coefficients (γ_0, γ_1, γ_2, and γ_3) in equation (15) for each of the groups. We obtain three different models, incorporating seasonal fluctuations function of the characteristic ϕ_{50} of each transect. For the backshore slope ($H{:}V$; $\cot(\beta_b)$), the correlation coefficient obtained with the model proposed is $rho = 0.74$, the bias $BIAS = 0.0$, and the RMS error $RMS = 18.86$. The imposed seasonal cycle in the backshore slope model improves the quality of the regression model and has a high impact on the modeled FDE.

Appendix C: Numerical Implementation

The proposed model uses finite differences for the space discretization. Spatial discretization in long-term coastal evolution models is usually transect based (Vitousek, Barnard, Limber, Erikson, et al., 2017), grid based (Ashton & Murray, 2006a), or vector based (Hurst et al., 2015). We discretized the coastline into shore-normal transects spaced in alongshore direction to facilitate the composition of the different process-driven models in equations (1)–(3). The shoreline position at a given time step is measured by the distance, Y_S, from the onshore end of each transect. COCOONED computes the evolution of Y_S for each transect (Figure 5). Accordingly, the shoreline evolves on each transect. The FDE volume, V_D, is computed from the retreat of the foredune position, Y_D, which also evolves on the same transects as the shoreline position (Figure 5). The model domain and the transects are shown in Figure 6. The averaged shoreline from the observations is represented by the white line in Figure 6. We adapt the orientation of the transects to be normal to the purple line in the same figure, which defines the long-term averaged shoreline orientation produced by the nearshore hindcast wave climate (see section 3.1). This new averaged shoreline is computed with the alongshore model proposed by Anderson et al. (2018) running the recent hindcast wave climate for 500 years, and it represents a numerical shoreline overcoming defects inherited from the wave climate, for example, the BIAS present on the wave direction in the offshore reanalysis (see Table 1) and wave propagation. For example, we have not included the wave shadowing and refraction by the southern shoals and the jetty near Gray Harbor mouth during the propagation from the 20-m contour to wave breaking.

For time discretization COCOONED uses a two-level time stepping scheme, a finite difference discretization of the time derivative called Standard $\Omega-$ *scheme*. Equations (1)–(3) are written then,

$$\begin{aligned}\frac{(Y_S)_k^{n+1}-(Y_S)_k^n}{\Delta t} = \Bigg[\Omega\Bigg(&\frac{-1}{d_k}\frac{(Q_L)_{k+1/2}^{n+1}-(Q_L)_{k-1/2}^{n+1}}{\Delta x_k}+(K_C)_k^{n+1}\left((Y_{S,eq})_k^{n+1}-(Y_S)_k^{n+1}\right)\\&+\frac{-1}{d_k}\left(\frac{(SV_x)_{k+1/2}^{n+1}-(SV_x)_{k-1/2}^{n+1}}{\Delta x_k}+\frac{(\Delta SV_y)_k^{n+1}}{\Delta x_k}\right)\Bigg)\\&+(1-\Omega)\Bigg(\frac{-1}{d_k}\frac{(Q_L)_{k+1/2}^{n}-(Q_L)_{k-1/2}^{n}}{\Delta x_k}+(K_C)_k^{n}\left((Y_{S,eq})_k^{n}-(Y_S)_k^{n}\right)\\&+\frac{-1}{d_k}\left(\frac{(SV_x)_{k+1/2}^{n}-(SV_x)_{k-1/2}^{n}}{\Delta x_k}+\frac{(\Delta SV_y)_k^{n}}{\Delta x_k}\right)\Bigg)\Bigg],\end{aligned} \tag{C1}$$

$$\begin{aligned}\frac{(V_D)_k^{n+1}-(V_D)_k^n}{\Delta t} = \Bigg[\Omega\Bigg(&\left((Z_{D,toe})_k^{n+1}-TWL_k^{n+1}\right)\frac{(Y_{D,eq})_k^{n+1}-(Y_D)_k^{n+1}}{(T_s)_k^{n+1}}\Bigg)+\\&(1-\Omega)\left(\left((Z_{D,toe})_k^{n}-TWL_k^{n}\right)\frac{(Y_{D,eq})_k^{n}-(Y_D)_k^{n}}{(T_s)_k^{n}}\right)\Bigg],\end{aligned} \tag{C2}$$

where k represents the transect index, superscripts n represents the time step index, Δt is the time step, and Δx_k is the distance between adjacent transects. All of COCOONED parameters and variables in equations (C1) and (C2) are defined at each transect (with index k) except the longshore transport rate, Q,

which is located between adjacent transects (with indices $k \pm 1/2$; see Figure 5). Ω represents the implicitness parameter and takes values in between 0 and 1. Below, we summarize three potential schemes according to the Ω value.

$$\begin{aligned} \Omega = 0 \quad & forward\ Euler\ scheme \quad explicit, \quad \mathcal{O}(\Delta t); \\ \Omega = 1/2 \quad & Crank - Nicholson\ scheme \quad implicit, \quad \mathcal{O}(\Delta t)^2; \\ \Omega = 1 \quad & backward\ Euler\ scheme \quad implicit, \quad \mathcal{O}(\Delta t). \end{aligned}$$

Note that by taking a value of $\Omega = 1/2$ in the absence of LST (waves perpendicular to the coastline) and sediment supply, equation (C1) is reduced to the same equation presented in Miller and Dean (2004). Implicit schemes are proven to be more stable over a wide range of time steps, sometimes unconditionally, and they constitute excellent iterative solvers (Antolínez et al., 2016; Vitousek & Barnard, 2015). However, at large Δt they can be insufficiently accurate, and convergence of linear solvers can deteriorate or fail. For this reason and because of the size of the problem, we use a Jacobian Free Newton Krylov method (Baker et al., 2005; Knoll & Keyes, 2004) for solving equations (C1) and (C2). This numerical implementation in combination with proper input reduction and acceleration techniques can reduce the computational time while keeping the accuracy of the solution as presented in Antolínez et al. (2016).

Acknowledgments
We thank Katherine A. Serafin for extracting the water level components from the tidal gauge. We thank Nicholas Cohn for the initial SWAN setup for the nearshore propagation of waves and the further discussion on its optimization in our application. We thank the three anonymous reviewers and editors for their careful reading of our manuscript and their many insightful comments and suggestions. J. A. A. Antolínez is indebted to the MEC (Ministerio de Educación, Cultura y Deporte, Spain) for the funding provided in the FPU (Formación del Profesorado Universitario) studentship (BOE-A-2013-12235). J. A. A. Antolínez and F. J. Méndez acknowledge the support of the Spanish "Ministerio de Economia y Competitividad" under Grant BIA2014-59643-R. P. Ruggiero and D. Anderson thank the NOAA Regional Integrated Sciences and Assessment (RISA) Program from NOAA's Climate Program Office under cooperative agreement NA15OAR431014 and NOAA's Coastal and Ocean Climate Applications (COCA) program under Grant NA15OAR4310243 for supporting their contributions to this work. Field data collection of the topographic profiles (Ruggiero et al., 2005) was also funded in part by the Northwest Association of Networked Ocean Observing Systems (http://nvs.nanoos.org/BeachMapping). Wave data are obtained from Global Ocean Waves (GOW2, Perez et al., 2017). Tide gauge and buoy records are available through the National Oceanic and Atmospheric Administration (NOAA) National Ocean Service (NOS; https://co-ops.nos.noaa.gov) website and National Data Buoy Center (NDBC; https://www.ndbc.noaa.gov).

References

Aagaard, T. (2014). Sediment supply to beaches: Cross-shore sand transport on the lower shoreface. *Journal of Geophysical Research: Earth Surface*, *119*, 913–926. https://doi.org/10.1002/2013JF003041

Anderson, D., Ruggiero, P., Antolínez, J. A. A., Méndez, F. J., & Allan, J. (2018). A climate index optimized for longshore sediment transport reveals interannual and multi-decadal littoral cell rotations. *Journal of Geophysical Research: Earth Surface*, *123*, 1958–1981. https://doi.org/10.1029/2018JF004689

Antolínez, J. A. A., Méndez, F. J., Camus, P., Vitousek, S., González, E. M., Ruggiero, P., & Barnard, P. (2016). A multiscale climate emulator for longterm morphodynamics (MUSCLEmorpho). *Journal of Geophysical Research: Oceans*, *121*, 775–791. https://doi.org/10.1002/2015JC011107

Antolínez, J. A. A., Murray, A. B., Méndez, F. J., Moore, L. J., Farley, G., & Wood, J. (2018). Downscaling changing coastlines in a changing climate: The hybrid approach. *Journal of Geophysical Research: Earth Surface*, *123*, 229–251. https://doi.org/10.1002/2017JF004367

Arriaga, J., Rutten, J., Ribas, F., Falqués, A., & Ruessink, G. (2017). Modeling the long-term diffusion and feeding capability of a mega-nourishment. *Coastal Engineering*, *121*, 1–13. https://doi.org/10.1016/j.coastaleng.2016.11.011

Ashton, A. D., & Murray, A. B. (2006a). High-angle wave instability and emergent shoreline shapes: 1. Modeling of sand waves, flying spits, and capes. *Journal of Geophysical Research*, *111*, F04011. https://doi.org/10.1029/2005JF000422

Ashton, A. D., & Murray, A. B. (2006b). High-angle wave instability and emergent shoreline shapes: 2. Wave climate analysis and comparisons to nature. *Journal of Geophysical Research*, *111*, F04012. https://doi.org/10.1029/2005JF000423

Ashton, A., Murray, A. B., & Arnoult, O. (2001). Formation of coastline features by large-scale instabilities induced by high-angle waves. *Nature*, *414*(6861), 296–300.

Ashton, A., Murray, A. B., & Arnoult, O. (2002). Erratum: Formation of coastline features by large-scale instabilities induced by high-angle waves. *Nature*, *415*(6872), 666–666. https://doi.org/10.1038/415666a

Aubrey, D. G. (1979). Seasonal patterns of onshore/offshore sediment movement. *Journal of Geophysical Research*, *84*(C10), 6347–6354. https://doi.org/10.1029/JC084iC10p06347

Baker, A. H., Jessup, E. R., & Manteuffel, T. (2005). A technique for accelerating the convergence of restarted gmres. *SIAM Journal on Matrix Analysis and Applications*, *26*(4), 962–984. https://doi.org/10.1137/S0895479803422014

Barnard, P. L., Hoover, D., Hubbard, D. M., Snyder, A., Ludka, B. C., Allan, J., et al. (2017). Extreme oceanographic forcing and coastal response due to the 2015-2016 El Niño. *Nature Communications*, *8*, 14365.

Barnard, P. L., Hubbard, D. M., & Dugan, J. E. (2012). Beach response dynamics of a littoral cell using a 17-year single-point time series of sand thickness. *Geomorphology*, *139-140*, 588–598. https://doi.org/10.1016/j.geomorph.2011.12.023

Bayram, A., Larson, M., & Hanson, H. (2007). A new formula for the total longshore sediment transport rate. *Coastal Engineering*, *54*(9), 700–710. https://doi.org/10.1016/j.coastaleng.2007.04.001

Beets, D. J., & van der Spek, A. J. F. (2000). The holocene evolution of the barrier and the back-barrier basins of belgium and the netherlands as a function of late weichselian morphology, relative sea-level rise and sediment supply. *Netherlands Journal of Geosciences - Geologie en Mijnbouw*, *79*(1), 3–16. https://doi.org/10.1017/S0016774600021533

Biel, R. G., Hacker, S. D., Ruggiero, P., Cohn, N., & Seabloom, E. W. (2017). Coastal protection and conservation on sandy beaches and dunes: context-dependent tradeoffs in ecosystem service supply. *Ecosphere*, *8*(4), e01791. https://doi.org/10.1002/ecs2.1791

Birkemeier, W. A. (1985). Field data on seaward limit of profile change. *Journal of Waterway, Port, Coastal, and Ocean Engineering*, *111*(3), 598–602. https://doi.org/10.1061/(ASCE)0733-950X(1985)111:3(598)

Blossier, B., Bryan, K. R., Daly, C. J., & Winter, C. (2017). Shore and bar cross-shore migration, rotation, and breathing processes at an embayed beach. *Journal of Geophysical Research: Earth Surface*, *122*, 1745–1770. https://doi.org/10.1002/2017JF004227

Booij, N., Ris, R. C., & Holthuijsen, L. H. (1999). A third-generation wave model for coastal regions: 1. Model description and validation. *Journal of Geophysical Research*, *104*(C4), 7649–7666. https://doi.org/10.1029/98JC02622

Bromirski, P. D., Flick, R. E., & Cayan, D. R. (2003). Storminess variability along the california coast: 1858–2000. *Journal of Climate*, *16*(6), 982–993. https://doi.org/10.1175/1520-0442(2003)016<0982:SVATCC>2.0.CO;2

Bruun, P. (1962). Sea-level rise as a cause of shore erosion. *Journal of the Waterways and Harbors Division*, *88*(1), 117–132.

Buijsman, M., Kaminsky, G., & Gelfenbaum, G. (2003). Shoreline change associated with jetty construction, deterioration and rehabilitation at grays harbor, washington. *Shore and Beach*, *71*(1), 15–22.

Buijsman, M., Sherwood, C., Gibbs, A., Gelfenbaum, G., Kaminsky, G., Ruggiero, P., & Franklin, J. (2003). Regional sediment budget analysis of the Columbia River littoral cell. Open-File Report 2002-281 USGS. https://doi.org/10.3133/ofr02281

Callaghan, D. P., Ranasinghe, R., & Roelvink, D. (2013). Probabilistic estimation of storm erosion using analytical, semi-empirical, and process based storm erosion models. *Coastal Engineering*, *82*, 64–75. https://doi.org/10.1016/j.coastaleng.2013.08.007

Camus, P., Mendez, F. J., & Medina, R. (2011). A hybrid efficient method to downscale wave climate to coastal areas. *Coastal Engineering*, *58*(9), 851–862. https://doi.org/10.1016/j.coastaleng.2011.05.007

Carignan, K., Taylor, L., Eakins, B., & Warnken, R. (2009). Digital elevation model of Astoria, Oregon: Procedures, data sources and analysis. NOAA technical memorandum NESDIS NGDC; 22.

Cheng, Z., Hsu, T.-J., & Calantoni, J. (2017). Sedfoam: A multi-dimensional Eulerian two-phase model for sediment transport and its application to momentary bed failure. *Coastal Engineering*, *119*, 32–50. https://doi.org/10.1016/j.coastaleng.2016.08.007

Coco, G., Senechal, N., Rejas, A., Bryan, K., Capo, S., Parisot, J., et al. (2014). Beach response to a sequence of extreme storms. *Geomorphology*, *204*, 493–501. https://doi.org/10.1016/j.geomorph.2013.08.028

Cohn, N., Anderson, D., & Ruggiero, P. (2015). Observations of intertidal bar welding along a high energy, dissipative coastline. In P. Wang, J. D. Rosati, & J. Cheng (Eds.), *Coastal Sediments* (Vol. 2015, pp. 215). Singapore: World Scientific Publishing Co Pte Ltd. https://doi.org/10.1142/9789814689977_0021

Cohn, N., & Ruggiero, P. (2016). The influence of seasonal to interannual nearshore profile variability on extreme water levels: Modeling wave runup on dissipative beaches. *Coastal Engineering*, *115*, 79–92. https://doi.org/10.1016/j.coastaleng.2016.01.006, swash-zone Processes.

Cohn, N., Ruggiero, P., de Vries, S., & Kaminsky, G. M. (2018). New insights on coastal foredune growth: The relative contributions of marine and aeolian processes. *Geophysical Research Letters*, *45*, 4965–4973. https://doi.org/10.1029/2018GL077836

Cowell, P. J., Stive, M. J., Niedoroda, A. W., de Vriend, H. J., Swift, D. J., Kaminsky, G. M., & Capobianco, M. (2003). The coastal-tract (part 1): A conceptual approach to aggregated modeling of low-order coastal change. *Journal of Coastal Research*, *19*(4), 812–827.

Cowell, P. J., Stive, M. J., Niedoroda, A. W., Swift, D. J., de Vriend, H. J., Buijsman, M. C., et al. (2003). The coastal-tract (part 2): Applications of aggregated modeling of lower-order coastal change. *Journal of Coastal Research*, *19*(4), 828–848.

Cox, J., & Machemehl, J. (1986). Overland bore propagation due to an overtopping wave. *Journal of Waterway, Port, Coastal, and Ocean Engineering*, *112*(1), 161–163.

Davidson, M., Lewis, R., & Turner, I. (2010). Forecasting seasonal to multi-year shoreline change. *Coastal Engineering*, *57*(6), 620–629. https://doi.org/10.1016/j.coastaleng.2010.02.001

Davidson, M., Splinter, K., & Turner, I. (2013). A simple equilibrium model for predicting shoreline change. *Coastal Engineering*, *73*, 191–202. https://doi.org/10.1016/j.coastaleng.2012.11.002

de Vriend, H., Capobianco, M., Chesher, T., de Swart, H., Latteux, B., & Stive, M. (1993). Approaches to long-term modelling of coastal morphology: A review. *Coastal Engineering*, *21*(1-3), 225–269. https://doi.org/10.1016/0378-3839(93)90051-9

Dean, R. G. (1987). Coastal sediment processes: Toward engineering solutions. In *Proceedings of the Specialty Conference on Coastal Sediments '87*, American Society of Civil Engineers, Cambridge, pp. 1–24.

Dean, R. G. (1991). Equilibrium beach profiles: Characteristics and applications. *Journal of Coastal Research*, *7*(1), 53–84. https://doi.org/10.2307/4297805

Di Leonardo, D., & Ruggiero, P. (2015). Regional scale sandbar variability: Observations from the U. S. Pacific Northwest. *Continental Shelf Research*, *95*, 74–88. https://doi.org/10.1016/j.csr.2014.12.012

Dolan, R., Hayden, B., & Heywood, J. (1978). A new photogrammetric method for determining shoreline erosion. *Coastal Engineering*, *2*, 21–39. https://doi.org/10.1016/0378-3839(78)90003-0

Falqués, A., Ribas, F., Idier, D., & Arriaga, J. (2017). Formation mechanisms for self-organized km-scale shoreline sand waves. *Journal of Geophysical Research: Earth Surface*, *122*, 1121–1138. https://doi.org/10.1002/2016JF003964

Fenster, M., & Dolan, R. (1994). Large-scale reversals in shoreline trends along the U.S. mid-Atlantic coast. *Geology*, *22*, 543. https://doi.org/10.1130/0091-7613(1994)022<0543:LSRIST>2.3.CO;2

Franke, R. (1982). Scattered data interpolation: Tests of some methods. *Mathematics of Computation*, *38*(157), 181–181. https://doi.org/10.1090/S0025-5718-1982-0637296-4

French, J., Payo, A., Murray, B., Orford, J., Eliot, M., & Cowell, P. (2016). Appropriate complexity for the prediction of coastal and estuarine geomorphic behaviour at decadal to centennial scales. *Geomorphology*, *256*, 3–16. https://doi.org/10.1016/j.geomorph.2015.10.005

García-Medina, G., Özkan Haller, H. T., Ruggiero, P., & Oskamp, J. (2013). An inner-shelf wave forecasting system for the u.s. pacific northwest. *Weather and Forecasting*, *28*(3), 681–703. https://doi.org/10.1175/WAF-D-12-00055.1

Gelfenbaum, G., Sherwood, C., Peterson, C., Kaminsky, G., Buijsman, M., Twichell, D., et al. (1999). The Columbia River littoral cell: A sediment budget overview. In *Proceedings of Coastal Sediments '99*, American Society of Civil Engineers, Long Island, NY, pp. 1660–1675.

Hallermeier, R. J. (1980). A profile zonation for seasonal sand beaches from wave climate. *Coastal Engineering*, *4*(C), 253–277. https://doi.org/10.1016/0378-3839(80)90022-8

Hanson, H. (1989). Genesis: A generalized shoreline change numerical model. *Journal of Coastal Research*, *5*(1), 1–27.

Hanson, H., Larson, M., & Kraus, N. C. (2010). Calculation of beach change under interacting cross-shore and longshore processes. *Coastal Engineering*, *57*(6), 610–619. https://doi.org/10.1016/j.coastaleng.2010.02.002

Harley, M. D., Turner, I. L., & Short, A. D. (2015). New insights into embayed beach rotation: The importance of wave exposure and cross-shore processes. *Journal of Geophysical Research: Earth Surface*, *120*, 1470–1484. https://doi.org/10.1002/2014JF003390

Harley, M. D., Turner, I. L., Short, A. D., & Ranasinghe, R. (2011). A reevaluation of coastal embayment rotation: The dominance of cross-shore versus alongshore sediment transport processes, Collaroy-Narrabeen Beach, Southeast Australia. *Journal of Geophysical Research*, *116*, F04033. https://doi.org/10.1029/2011JF001989

Hartman, M., & Kennedy, A. B. (2016). Depth of closure over large regions using airborne bathymetric lidar. *Marine Geology*, *379*, 52–63. https://doi.org/10.1016/j.margeo.2016.05.012

Hurst, M. D., Barkwith, A., Ellis, M. A., Thomas, C. W., & Murray, A. B. (2015). Exploring the sensitivities of crenulate bay shorelines to wave climates using a new vector-based one-line model. *Journal of Geophysical Research: Earth Surface*, *120*, 2586–2608. https://doi.org/10.1002/2015JF003704.We

IPCC (2013). *Climate change 2013: The physical science basis. Contribution of Working Group I to the Fifth Assessment Report of the Intergovernmental Panel on Climate Change, Technical Summary* (pp. 33–115). Cambridge, United Kingdom and New York, NY, USA: Cambridge University Press. https://doi.org/10.1017/CBO9781107415324.005

Idier, D., Falqués, A., Ruessink, B. G., & Garnier, R. (2011). Shoreline instability under low-angle wave incidence. *Journal of Geophysical Research*, *116*, F04031. https://doi.org/10.1029/2010JF001894

Kaergaard, K., & Fredsoe, J. (2013a). Numerical modeling of shoreline undulations part 1: Constant wave climate. *Coastal Engineering*, *75*, 64–76. https://doi.org/10.1016/j.coastaleng.2012.11.006

Kaergaard, K., & Fredsoe, J. (2013b). Numerical modeling of shoreline undulations part 2: Varying wave climate and comparison with observations. *Coastal Engineering*, *75*, 77–90. https://doi.org/10.1016/j.coastaleng.2012.11.003

Kaminsky, G., Buijsman, M., & Ruggiero, P. (2001). Predicting shoreline change at decadal scale in the Pacific Northwest. In *Proceedings of The International Conference on Coastal Engineering*, American Society of Civil Engineers, Sydney, Australia, pp. 2000.

Kaminsky, G. M., & Ferland, M. (2003). Assessing the connections between the inner shelf and the evolution of Pacific Northwest barriers through vibracoring. In *International Conference on Coastal Sediments 2003*, American Society of Civil Engineers, Clearwater Beach, Florida, USA, ASCE. 12 pp.

Kaminsky, G. M., Ruggiero, P., Buijsman, M. C., McCandless, D., & Gelfenbaum, G. (2010). Historical evolution of the Columbia River littoral cell. *Marine Geology*, *273*(1-4), 96–126. https://doi.org/10.1016/j.margeo.2010.02.006

Kaminsky, G. M., Ruggiero, P., & Gelfenbaum, G. (1998). Monitoring coastal change in southwest Washington and northwest Oregon during the 1997/98 El Niño. *Shore & Beach*, *66*(3), 42–51.

Kamphuis, J. W. (1991). Alongshore sediment transport rate. *Journal of Waterway, Port, Coastal, and Ocean Engineering*, *117*(6), 624–640. https://doi.org/10.1061/(ASCE)0733-950X(1991)117:6(624)

Kildow, J., Colgan, C., & Scorse, J. (2014). State of the U. S. ocean and coastal economies 2014. Center for the Blue Economy at the Monterey Institute of International Studies, 1–84.

Kinsela, M. A., & Cowell, P. J. (2015). Controls on shoreface response to sea level change. In P. Wang, J. D. Rosati, & J. Cheng (Eds.), *Coastal Sediments* (Vol. 2015, pp. 204). Singapore: World Scientific Publishing Co Pte Ltd.

Knoll, D., & Keyes, D. (2004). Jacobian-free newton-krylov methods: A survey of approaches and applications. *Journal of Computational Physics*, *193*(2), 357–397. https://doi.org/10.1016/j.jcp.2003.08.010

Komar, P. D. (1971). The mechanics of sand transport on beaches. *Journal of Geophysical Research*, *76*(3), 713–721. https://doi.org/10.1029/JC076i003p00713

Komar, P. D., Allan*, J. C., & Ruggiero, P. (2011). Sea level variations along the U.S. Pacific Northwest Coast: Tectonic and climate controls. *Journal of Coastal Research*, *27*, 808–823. https://doi.org/10.2112/JCOASTRES-D-10-00116.1

Kriebel, D. L., & Dean, R. G. (1993). Convolution method for time-dependent beach-profile response. *Journal of Waterway, Port, Coastal, and Ocean Engineering*, *119*(2), 204–226. https://doi.org/10.1061/(ASCE)0733-950X(1993)119:2(204)

Kristensen, S., Drønen, N., Deigaard, R., & Fredsoe, J. (2016). Impact of groyne fields on the littoral drift: A hybrid morphological modelling study. *Coastal Engineering*, *111*, 13–22. https://doi.org/10.1016/j.coastaleng.2016.01.009

Larson, M., Palalane, J., Fredriksson, C., & Hanson, H. (2016). Simulating cross-shore material exchange at decadal scale. theory and model component validation. *Coastal Engineering*, *116*, 57–66.

Mil-Homens, J., Ranasinghe, R., van Thiel de Vries, J. S. M., & Stive, M. J. F. (2013). Re-evaluation and improvement of three commonly used bulk longshore sediment transport formulas. *Coastal Engineering*, *75*, 29–39. https://doi.org/10.1016/j.coastaleng.2013.01.004

Miller, J. K., & Dean, R. G. (2004). A simple new shoreline change model. *Coastal Engineering*, *51*(7), 531–556. https://doi.org/10.1016/j.coastaleng.2004.05.006

Miller, J. K., & Dean, R. G. (2007a). Shoreline variability via empirical orthogonal function analysis: Part I temporal and spatial characteristics. *Coastal Engineering*, *54*(2), 111–131. https://doi.org/10.1016/j.coastaleng.2006.08.013

Miller, J. K., & Dean, R. G. (2007b). Shoreline variability via empirical orthogonal function analysis: Part II relationship to nearshore conditions. *Coastal Engineering*, *54*(2), 133–150. https://doi.org/10.1016/j.coastaleng.2006.08.014

Moore, L. J., List, J. H., Williams, S. J., & Stolper, D. (2010). Complexities in barrier island response to sea level rise: Insights from numerical model experiments, north carolina outer banks. *Journal of Geophysical Research*, *115*, F03004. https://doi.org/10.1029/2009JF001299

Moore, L. J., McNamara, D. E., Murray, A. B., & Brenner, O. (2013). Observed changes in hurricane-driven waves explain the dynamics of modern cuspate shorelines. *Geophysical Research Letters*, *40*, 5867–5871. https://doi.org/10.1002/2013GL057311

Mull, J., & Ruggiero, P. (2014). Estimating storm-induced dune erosion and overtopping along u.s. west coast beaches. *Journal of Coastal Research*, *30*, 1173–1187. https://doi.org/10.2112/JCOASTRES-D-13-00178.1

Murray, A. B. (2007). Reducing model complexity for explanation and prediction. *Geomorphology*, *90*(3-4), 178–191. https://doi.org/10.1016/j.geomorph.2006.10.020

Murray, A. B., & Ashton, A. D. (2013). Instability and finite-amplitude self-organization of large-scale coastline shapes. *Philosophical Transactions of the Royal Society of London A: Mathematical, Physical and Engineering Sciences*, *371*(2004), 20120363. https://doi.org/10.1098/rsta.2012.0363

Neumann, B., Vafeidis, A. T., Zimmermann, J., & Nicholls, R. J. (2015). Future coastal population growth and exposure to sea-level rise and coastal flooding - a global assessment. *PLOS ONE*, *10*(3), 1–34. https://doi.org/10.1371/journal.pone.0118571

Nicholls, R. J., Birkemeier, W. A., & hong Lee, G. (1998). Evaluation of depth of closure using data from duck, nc, usa. *Marine Geology*, *148*(3), 179–201. https://doi.org/10.1016/S0025-3227(98)00011-5

Oertel, G. F. (1972). Sediment transport of estuary entrance shoals and the formation of swash platforms. *Journal of Sedimentary Research*, *42*, 858–863. https://doi.org/10.1306/74D72658-2B21-11D7-8648000102C1865D

Ortiz, A. C., & Ashton, A. D. (2016). Exploring shoreface dynamics and a mechanistic explanation for a morphodynamic depth of closure. *Journal of Geophysical Research: Earth Surface*, *121*, 442–464. https://doi.org/10.1002/2015JF003699.Received

Palalane, J., Fredriksson, C., Marinho, B., Larson, M., Hanson, H., & Coelho, C. (2016). Simulating cross-shore material exchange at decadal scale. model application. *Coastal Engineering*, *116*, 26–41. https://doi.org/10.1016/j.coastaleng.2016.05.007

Patterson, D. C., & Nielsen, P. (2016). Depth, bed slope and wave climate dependence of long term average sand transport across the lower shoreface. *Coastal Engineering*, *117*, 113–125. https://doi.org/10.1016/j.coastaleng.2016.07.007

Pedregosa, F., Varoquaux, G., Gramfort, A., Michel, V., Thirion, B., Grisel, O., et al. (2011). Scikit-learn: Machine learning in python. *Journal of Machine Learning Research*, *12*, 2825–2830.

Perez, J., Menendez, M., & Losada, I. J. (2017). Gow2: A global wave hindcast for coastal applications. *Coastal Engineering*, *124*, 1–11. https://doi.org/10.1016/j.coastaleng.2017.03.005

Ranasinghe, R., & Pattiaratchi, C. (1999). The seasonal closure of tidal inlets: Wilson inlet-a case study. *Coastal Engineering*, *37*(1), 37–56. https://doi.org/10.1016/S0378-3839(99)00007-1

Ranasinghe, R., & Stive, M. J. F. (2009). Rising seas and retreating coastlines. *Climatic Change*, *97*(3-4), 465–468. https://doi.org/10.1007/s10584-009-9593-3

Ratliff, K. M., & Murray, A. B. (2014). Modes and emergent time scales of embayed beach dynamics. *Geophysical Research Letters*, *41*, 7270–7275. https://doi.org/10.1002/2014GL061680

Rippa, S. (1999). An algorithm for selecting a good value for the parameter c in radial basis function interpolation. *Advances in Computational Mathematics*, *11*, 193–210. https://doi.org/10.1023/A:1018975909870

Robinet, A., Idier, D., Castelle, B., & Marieu, V. (2018). A reduced-complexity shoreline change model combining longshore and cross-shore processes: The lx-shore model. *Environmental Modelling & Software*, *109*, 1–16. https://doi.org/10.1016/j.envsoft.2018.08.010

Roelvink, J. (2006). Coastal morphodynamic evolution techniques. *Coastal Engineering*, *53*(2-3), 277–287. https://doi.org/10.1016/j.coastaleng.2005.10.015

Rosati, J., Dean, R., & Walton, T. (2013). The modified Bruun rule extended for landward transport. *Marine Geology*, *340*, 71–81. https://doi.org/10.1016/j.margeo.2013.04.018

Ruessink, B. G., Kuriyama, Y., Reniers, A. J. H. M., Roelvink, J. A., & Walstra, D. J. R. (2007). Modeling cross-shore sandbar behavior on the timescale of weeks. *Journal of Geophysical Research*, *112*, F03010. https://doi.org/10.1029/2006JF000730

Ruggiero, P., Buijsman, M., Kaminsky, G. M., & Gelfenbaum, G. (2010). Modeling the effects of wave climate and sediment supply variability on large-scale shoreline change. *Marine Geology*, *273*(1), 127–140. https://doi.org/10.1016/j.margeo.2010.02.008, large-scale coastal change in the Columbia River littoral cell.

Ruggiero, P., Kaminsky, G. M., Gelfenbaum, G., & Cohn, N. (2016). Morphodynamics of prograding beaches: A synthesis of seasonal- to century-scale observations of the Columbia River littoral cell. *Marine Geology*, *376*, 51–68. https://doi.org/10.1016/j.margeo.2016.03.012

Ruggiero, P., Kaminsky, G. M., Gelfenbaum, G., & Voigt, B. (2005). Seasonal to interannual morphodynamics along a high-energy dissipative littoral cell. *Journal of Coastal Research*, *21*, 553–578. https://doi.org/10.2112/03-0029.1

Ruggiero, P., Komar, P. D., & Allan, J. C. (2010). Increasing wave heights and extreme value projections: The wave climate of the u.s. pacific northwest. *Coastal Engineering*, *57*(5), 539–552. https://doi.org/10.1016/j.coastaleng.2009.12.005

Ruggiero, P., Kratzmann, M. G., Himmelstoss, E. A., Reid, D., Allan, J., & Kaminsky, G. M. (2013). National assessment of shoreline change: Historical shoreline change along the Pacific Northwest Coast. Reston, VA.

Sallenger, A. H. J. (2000). Storm impact scale for barrier islands. *Journal of Coastal Research*, *16*(3), 890–895.

Seabloom, E. W., Ruggiero, P., Hacker, S. D., Mull, J., & Zarnetske, P. (2012). Invasive grasses, climate change, and exposure to storm-wave overtopping in coastal dune ecosystems. *Global Change Biology*, *19*(3), 824–832. https://doi.org/10.1111/gcb.12078

Serafin, K. A., Ruggiero, P., & Stockdon, H. F. (2017). The relative contribution of waves, tides, and nontidal residuals to extreme total water levels on u.s. west coast sandy beaches. *Geophysical Research Letters*, *44*, 1839–1847. https://doi.org/10.1002/2016GL071020

Splinter, K. D., Turner, I. L., & Davidson, M. A. (2013). How much data is enough? The importance of morphological sampling interval and duration for calibration of empirical shoreline models. *Coastal Engineering*, *77*, 14–27. https://doi.org/10.1016/j.coastaleng.2013.02.009

Splinter, K. D., Turner, I. L., Davidson, M. A., Barnard, P., Castelle, B., & Oltman-Shay, J. (2014). A generalized equilibrium model for predicting daily to interannual shoreline response. *Journal of Geophysical Research: Earth Surface*, *119*, 1936–1958. https://doi.org/10.1002/2014JF003106

Stockdon, H. F., Holman, R. A., Howd, P. A., & Sallenger, A. H. (2006). Empirical parameterization of setup, swash, and runup. *Coastal Engineering*, *53*(7), 573–588. https://doi.org/10.1016/j.coastaleng.2005.12.005

Storlazzi, C., & Field, M. (2000). Sediment distribution and transport along a rocky, embayed coast: Monterey peninsula and carmel bay, california. *Marine Geology*, *170*(3), 289–316. https://doi.org/10.1016/S0025-3227(00)00100-6

Tetra Tech, I., Authority, P. S. W. Q., & Program, P. S. E. (1986). Recommended protocols for measuring conventional sediment variables in Puget Sound, Recommended protocols for measuring selected environmental variables in Puget Sound, Puget Sound Water Quality Authority (PO Box 40900, Olympia, WA 98504-0900).

Tonnon, P., Huisman, B., Stam, G., & van Rijn, L. (2018). Numerical modelling of erosion rates, life span and maintenance volumes of mega nourishments. *Coastal Engineering*, *131*, 51–69. https://doi.org/10.1016/j.coastaleng.2017.10.001

van Rijn, L. C. (2014). A simple general expression for longshore transport of sand, gravel and shingle. *Coastal Engineering*, *90*, 23–39. https://doi.org/10.1016/j.coastaleng.2014.04.008

van de Lageweg, W., Bryan, K., Coco, G., & Ruessink, B. (2013). Observations of shoreline-sandbar coupling on an embayed beach. *Marine Geology*, *344*, 101–114. https://doi.org/10.1016/j.margeo.2013.07.018

Vitousek, S., & Barnard, P. L. (2015). A nonlinear, implicit one-line model to predict long-term shoreline change. In P. Wang, J. D. Rosati, & J. Cheng (Eds.), *Coastal Sediments* (Vol. 2015, pp. 215). Singapore: World Scientific Publishing Co Pte Ltd. https://doi.org/10.1142/9789814689977_0215

Vitousek, S., Barnard, P. L., & Limber, P. (2017). Can beaches survive climate change? *Journal of Geophysical Research: Earth Surface*, *122*, 1060–1067. https://doi.org/10.1002/2017JF004308

Vitousek, S., Barnard, P. L., Limber, P., Erikson, L., & Cole, B. (2017). A model integrating longshore and cros-shore processes for predicting long-term shoreline response to climate change. *Journal of Geophysical Research: Earth Surface*, *122*, 782–806. https://doi.org/10.1002/2016JF004065

Walstra, D. J. R., Hoekstra, R., Tonnon, P. K., & Ruessink, B. G. (2013). Input reduction for long-term morphodynamic simulations in wave-dominated coastal settings. *Coastal Engineering*, *77*(0), 57–70. https://doi.org/10.1016/j.coastaleng.2013.02.001

Walstra, D., Reniers, A., Ranasinghe, R., Roelvink, J., & Ruessink, B. (2012). On bar growth and decay during interannual net offshore migration. *Coastal Engineering*, *60*, 190–200. https://doi.org/10.1016/j.coastaleng.2011.10.002

Wentworth, C. K. (1922). A scale of grade and class terms for clastic sediments. *The Journal of Geology*, *30*(5), 377–392.

Wolinsky, M. a., & Murray, a. B. (2009). A unifying framework for shoreline migration: 2. Application to wave-dominated coasts. *Journal of Geophysical Research*, *114*, F01009. https://doi.org/10.1029/2007JF000856

Yates, M. L., Guza, R. T., & O'Reilly, W. C. (2009). Equilibrium shoreline response: Observations and modeling. *Journal of Geophysical Research*, *114*, C09014. https://doi.org/10.1029/2009JC005359

Yates, M. L., Guza, R. T., O'Reilly, W. C., Hansen, J. E., & Barnard, P. L. (2010). Equilibrium shoreline response of a high wave energy beach. *Journal of Geophysical Research*, *116*, C04014. https://doi.org/10.1029/2010JC006681